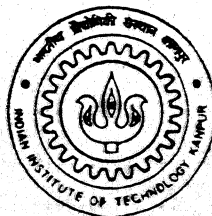


Analysis of Residual Stresses In 3-D Forging Using FEM

by

Samshette Shivkumar Umashankar



DEPARTMENT OF MECHANICAL ENGINEERING

INDIAN INSTITUTE OF TECHNOLOGY KANPUR

March, 1999

TH

ME/1999/m

Sa49a

ANALYSIS OF RESIDUAL STRESSES IN 3-D FORGING USING FEM

A Thesis Submitted
in Partial Fulfillment of the Requirements
for the Degree of
MASTER OF TECHNOLOGY

by
Samshette Shivkumar Umashankar




to the
DEPARTMENT OF MECHANICAL ENGINEERING
INDIAN INSTITUTE OF TECHNOLOGY KANPUR
MARCH, 1999



CERTIFICATE

It is certified that the work contained in the thesis entitled "**Analysis of Residual Stresses in 3-D Forging Using FEM**", by Samshette Shivkumar Umashankar, has been carried out under my supervision and that this work has not been submitted elsewhere for a degree.



P.M. Dixit
Professor
Department of Mechanical Engineering
I.I.T., Kanpur

March, 1999.

19 MAY 1999 *IME*
***CENTRAL LIBRARY**
I. I. T., KANPUR

Acc. No. A 127927

TH
MS/1999/m
Sa49a

Acknowledgements

I wish to place on record my deep sense of gratitude and indebtedness to Dr. P. M. Dixit for his guidance and encouragement during the course of my thesis work.

Sincere thanks are due to Kulkarni Santosh, R. Yogesh, Desai, S. Anil, T. Ganesh, D. Abhijit, Neeraj, Shiva Prasad and other my friends for their active support during the course of this work.

The financial support provided by C. S. I. R. is gratefully acknowledged.

Samshette Shivkumar U.

Contents

Certificate	i
Acknowledgements	iii
Abstract	iv
List of Figures	viii
List of Symbols	x
1 Introduction	1
1.1 Literature Survey	3
1.2 Modelling of Cold Forging Process	8
1.3 Objective	9
1.4 Plan of The Thesis	9
2 Mathematical Modelling and Finite Element Formulation of 3-D Forging Process	11
2.1 Updated Lagrangian Formulation	11
2.2 Kinematics of Finite Deformation	13
2.3 Stress Measures	14

2.4	Strain Measures	17
2.5	Elastic Constitutive Equation	18
2.6	Elasto-plastic Constitutive Equation	19
2.7	Incremental Updated Lagrangian Formulation	23
2.8	Finite Element Formulation	26
2.8.1	Matrix Notation	26
2.8.2	Finite Element Equation	28
2.8.3	Determination of Stresses	31
2.8.4	Integration of the Constitutive Equation	32
2.8.5	Unloading Scheme	33
2.9	Numerical Scheme	34
2.9.1	Modified Newton-Raphson Scheme	34
2.9.2	Arc Length Method	35
2.9.3	Numerical Integration Scheme	38
2.9.4	Divergence Procedures	39
2.10	Boundary Conditions for 3-D Forging of Rectangular Block . . .	41
3	Results And Discussion	44
3.1	Convergence Study	45
3.1.1	Convergence of Forging Load	46
3.1.2	Convergence of Stress Distribution	48
3.2	Validation	57
3.3	Analysis of Forging Parameters for Typical Case	59
3.4	Parametric Study	63
3.4.1	Effects of Geometric Ratios (h/a and b/a)	63
3.4.2	Effect of Percentage Reduction in Height	68

2.4	Strain Measures	17
2.5	Elastic Constitutive Equation	18
2.6	Elasto-plastic Constitutive Equation	19
2.7	Incremental Updated Lagrangian Formulation	23
2.8	Finite Element Formulation	26
2.8.1	Matrix Notation	26
2.8.2	Finite Element Equation	28
2.8.3	Determination of Stresses	31
2.8.4	Integration of the Constitutive Equation	32
2.8.5	Unloading Scheme	33
2.9	Numerical Scheme	34
2.9.1	Modified Newton-Raphson Scheme	34
2.9.2	Arc Length Method	35
2.9.3	Numerical Integration Scheme	38
2.9.4	Divergence Procedures	39
2.10	Boundary Conditions for 3-D Forging of Rectangular Block . . .	41
3	Results And Discussion	44
3.1	Convergence Study	45
3.1.1	Convergence of Forging Load	46
3.1.2	Convergence of Stress Distribution	48
3.2	Validation	57
3.3	Analysis of Forging Parameters for Typical Case	59
3.4	Parametric Study	63
3.4.1	Effects of Geometric Ratios (h/a and b/a)	63
3.4.2	Effect of Percentage Reduction in Height	68

3.4.3 Effect of Material Properties	70
4 Conclusions and Scope for Future work	73
References	75

List of Figures

2.1	Fixed and material reference frames	15
2.2	Boundary conditions for forging of a 3-D Rectangular Block . .	41
3.1	The domain used for analysis	46
3.2	Convergence with mesh size	47
3.3	Convergence with increment size	48
3.4	Equivalent stress distribution after 20 % reduction in (a) x_y (b) y_z planes for $5 \times 5 \times 6$ elements and increment size of 0.025 mm	49
3.5	Equivalent stress distribution after 20 % reduction in (a) x_y (b) y_z planes for $5 \times 5 \times 12$ elements and increment size of 0.025 mm	50
3.6	Equivalent stress distribution after 20 % reduction in (a) x_y (b) y_z planes for $10 \times 10 \times 12$ elements and increment size of 0.025 mm	51
3.7	Equivalent stress distribution after 20 % reduction in (a) x_y (b) y_z planes for $5 \times 5 \times 12$ elements and increment size of 0.0125 mm	52
3.8	Residual equivalent stress distribution after unloading in (a) x_y (b) y_z planes for $5 \times 5 \times 6$ elements and increment size of 0.025 mm	54
3.9	Residual equivalent stress distribution after unloading in (a) x_y (b) y_z planes for $5 \times 5 \times 12$ elements and increment size of 0.025 mm	55

3.10 Residual equivalent stress distribution after unloading in (a) x-y (b) y-z planes for $10 \times 10 \times 12$ elements and increment size of 0.025 mm	56
3.11 Residual equivalent stress distribution after unloading in (a) x-y (b) y-z planes for $5 \times 5 \times 12$ elements and increment size of 0.0125 mm	57
3.12 Comparison of theoretical and experimental [28] load-displacement curves.	58
3.13 distribution of contact pressure	60
3.14 bulge profile after loading	61
3.15 bulge profile after unloading	62
3.16 Equivalent stress distribution after 20 % reduction in y-z plane for $h/a=0.6$	64
3.17 Equivalent stress distribution after 20 % reduction in (a) y-z (b) x-z planes for $b/a=0.6$	65
3.18 Residual equivalent stress distribution after unloading in x-y plane for $h/a=0.6$	66
3.19 Residual equivalent stress distribution after unloading in y-z plane for $h/a=0.6$	66
3.20 Residual equivalent stress distribution after unloading in x-y plane for $b/a = 0.6$	67
3.21 Residual equivalent stress distribution after unloading in (a) y-z (b) x-z planes for $b/a = 0.6$	67
3.22 Residual equivalent stress distribution after unloading in x-y plane for 10 %reduction	69
3.23 Residual equivalent stress distribution after unloading in y-z plane for 10 %reduction	69
3.24 Equivalent stress distribution after 20 % reduction for steel in (a) x-y (b) y-z planes	71
3.25 Residual equivalent stress distribution after unloading for steel in (a) x-y (b) y-z planes	72

List of Symbols

$\{a\}$	Flow vector
$[B_L]$	Linear strain displacement matrix.
$[B_N]$	Non-linear strain displacement matrix.
C^E	Fourth order elasticity tensor
C^{EP}	Fourth order elastic-plastic tensor
$[C^E]$	Elasticity matrix
$[C^{EP}]$	Elasto-plastic matrix
e, e_{ij}	Green-Lagrange strain tensor, component
E	Young's Modulus
$f(), F()$	Generic representation of functions
f_i^S	Surface force component
$\{f\}$	Global internal Force vector
F, F_{ij}	Deformation gradient tensor, component
$[F]$	Matrix representation of Deformation gradient tensor
$\{F\}$	Global external force vector
$\{R\}$	Unbalance force vector
K	hardening coefficient

$[K]$	stiffness matrix
$[K_L]$	Linear part of the Stiffness matrix
$[K_N]$	Non-Linear part of the Stiffness matrix
n	Hardening exponent
N_i	Shape function
$\{P\}$	Basic load vector
N_i	Shape function
$[Q], Q_{ij}$	Transformation matrix, component
\mathbf{R}, R_{ij}	Rotation tensor, component
$[R]$	Matrix representation of components of R
\mathbf{S}, S_{ij}	Second Piola-Kirchoff stress tensor, component
$[S]$	Matrix representation of components of S
S_f	Surface with traction applied
tol_c	Tolerance for convergence of the numerical method
$\{u\}$	Displacement vector
$\{\Delta u^I\}$	Displacement vector due to the basic load vector
$\{\Delta u^{II}\}$	Displacement vector due to the unbalanced force vector
\mathbf{U}, U_{ij}	Right stretch tensor, component
$[U]$	Matrix of Right stretch tensor
$[U^P], U_{ij}^P$	Matrix representation of the components of U with respect to principal axes, component
V	Volume
\mathbf{W}, W_{ij}	Spin tensor, component
x_i	Co-ordinate of a generic particle
δ	Variation

δ_{ij}	Kronecker delta
Δ	Increment in quantity
ϵ, ϵ_{ij}	Small strain tensor, component
$[\epsilon]$	Matrix representation of ϵ
ϵ_{eq}^p	Equivalent plastic strain
$[\epsilon^L], \epsilon_{ij}^L$	Matrix representation of the components of the logarithmic strain tensor with respect to principal axes, component
$\epsilon^{pL}, \epsilon_{ij}^{pL}$	Plastic part of $[\epsilon^L]$, component
η, η_{ij}	Non-linear part of the Green-Lagrange strain tensor, component
λ_i	Principal stretch component
λ, μ	Lame's constants
$\Delta\lambda$	Load factor in arc length method
ν	poisson's ratio
ρ	Density
σ, σ_{ij}	Cauchy stress tensor, component
$[\sigma]$	Matrix representation of σ
$\dot{\sigma}, \dot{\sigma}_{ij}$	Cauchy stress rate tensor, component
σ^o, σ_{ij}^o	Jaumann stress rate tensor, component
σ_y	Yield stress
$[\sigma^M], \sigma_{ij}^M$	Matrix representation of the components of the stress tensor with respect to a material frame, component
σ', σ'_{ij}	Deviatoric part of the Cauchy stress tensor, component
$\{\Phi_i\}$	Array of shape functions

Chapter 1

Introduction

In forging, the material is squeezed between two or more dies in such a way that the metal or alloy is plastically deformed to the desired shape and size. It is also used to improve the metallurgical and mechanical properties of the material. This is the oldest of the metal working processes known to mankind since the copper age.

Generally the forging is performed by heating the material and then applying a compressive force to obtain the final shape. This is called the hot forging. The cold forging operation is carried out at room temperature. The forging operation is carried out in two different ways : drawing out and upsetting.

There are four types of forging methods which are generally used.

Smith forging- This is the traditional forging operation done openly or in open dies by a black smith, by manual hammering or by power hammers.

Drop forging - This is the operation done in closed impression dies by means of the drop hammers.

Press forging- Similar to drop forging, the press forging is also done in closed impression dies with the exception that the force is a continuous squeezing type applied by the hydraulic presses.

Machine forging- Unlike the drop or press forging where the material is drawn out, in machine forging, the material is only upset to get the desired shape.

A majority of the finished products made by forging are geometrically complex and the metal flow involved is of a three-dimensional nature. Thus, any technique of analysis will become more useful for problems of industrial importance, if it is capable of solving three dimensional metal flow problems.

Residual stresses are self-equilibrating internal stresses existing in a body after the removal of external forces and are caused by non-uniform deformation. It is generally believed that poor shape or bad surface finish of the work-piece is caused by residual stresses. Further, a tensile residual stress field near the surface can cause a micro-crack to propagate rapidly. Experimental methods for determination of residual stresses have been developed and used [1]. However, when the process is to be optimized, experimental methods do not provide an economical solution. Therefore, it is necessary to determine them by analytical or numerical methods. To calculate residual stresses in forging, a large deformation elasto-plastic finite element analysis, based on the updated Lagrangian formulation, needs to be carried out.

1.1 Literature Survey

The problem of upsetting of metals has theoretical as well as technological significance in that solutions would help to bring about a better understanding of the behavior of metals during plastic deformation at high pressure. Such solutions would give specific answers to problems actually encountered in practice. It is for these reasons that a number of investigators have dealt with the forging problem. Early investigators considered the material as an ideal plastic solid. This leads to so-called slip line solution. Such solutions have been proposed by Prandtl [2], Hill et al. [3], and Green [4]. The slip line theory has been well developed to analyse a non-homogeneous plane strain deformation of a rigid-perfectly plastic isotropic solid. This theory can be used to get very good first-approximations to loads required for performing operations and provide indications of the manner in which material deforms. However, the elastic and work hardening effects can not be incorporated in this method. Therefore a detailed solution for the deformation that takes place during continued loading beyond the yield point can not be obtained using this technique. Further, residual stresses also cannot be studied using this technique. Shabaik [5] investigated the bulging in upsetting by using the slipline theory.

Hoffman and Sach [6] proposed the slab method. A complete analysis of the slab method has been presented by Altan [7] for the axisymmetric closed die forging. In this method, a slab of infinitesimal thickness is selected and the equation representing the force equilibrium for the slab is derived, assuming that the deformation is homogeneous within the slab and that the major

directions are the principal stress directions. The resulting differential equation is then solved with appropriate boundary conditions. While this method can give very good predictions of the load variation with deformation, it is inherently incapable of predicting shape changes such as barreling in open die forging. Further, since the method is primarily based on the assumption of homogeneous deformation, it possibly cannot predict the residual stresses as they are caused only by non-uniform deformation.

The upper bound theorem was formulated by Prager and Hodge [8]. If surfaces of velocity discontinuities are included [9], then it states that among all kinematically admissible velocity fields v_i^* , the actual one minimizes the following expression

$$J^* = \int_V S_{ij}^* \dot{\epsilon}_{ij}^* dV + \int_{S_r} \tau |\Delta v^*| ds - \int_{S_t} T_i v_i^* ds \quad (1.1)$$

Here $\dot{\epsilon}_{ij}^*$ is the strain rate field derived from v_i^* , S_{ij}^* is the deviatoric stress field derived from $\dot{\epsilon}_{ij}^*$ and $|\Delta v^*|$ is the discontinuity in the tangential component of the velocity across the surface S_r . Further τ denotes the shear stress on the surface S_r and T_i is the prescribed traction on the part S_t of the boundary. The first term expresses the power spent in causing the internal deformation over the volume V of deforming body. The second term represents the power loss over the surfaces of velocity discontinuities including the boundary between tool and material. The last term represents the power supplied by specified tractions. What the upper bound theorem states is that the actual externally supplied power is never higher than that computed by the first two terms of the above equation.

Kudo [10] applied the upper bound theorem to the problems of axisymmetric cold forging and extrusion. Kudo [11] also applied the upper bound theorem to the analyses of the plane strain forging and extrusion. Avitzur [12], Kobayashi [13], McDonald et al. [14] and many others have suggested upper bound velocity fields to predict the forming load in upsetting with bulging. Yang and Kim [15], Kim et al. [16] and Marques and Martins [17] proposed upper bound method for analysis of three dimensional upset forging. The major difficulty in using the upper bound method is how to choose the kinematically admissible velocity field since the accuracy of the solution depends on how close the assumed velocity field is to the actual one. Another disadvantage of this method is that the solution provided by the method does not satisfy the equilibrium equations. So, even if elastic effects are included in integral (1.1), the method possibly can not be used for determination of residual stresses.

Accurate determination of forging parameters under realistic conditions became possible when the finite element method was introduced. The major advantage of the finite element method is that the method can be applied to a wide class of boundary value problems without restrictions on workpiece geometry used in the finite element method. Using FEM, it is possible to predict the platen forces, the interface pressure and the stress, strain and residual stress distributions within the billet at various deformation levels.

Early applications of the FEM to forging problems were based on the incremental method proposed by Lee and Kobayashi [18]. The method uses the elastic-plastic stress strain matrix based on Prandtl-Reuss equations. The additivity of incremental elastic and plastic strains is assumed. Even though

the stress-strain matrix and the geometry are updated after every increment. only the linearized incremental equations are used. The method was applied to solid cylinder upsetting [19], ring compression [20] and for predicting defects in upsetting [21]. Maccarini et al. [22] used the method for studying the influence of die geometry on cold extrusion forging operation. Where as Lee and Kobayashi [18] used the velocity as the primary unknown, Hartley et al. [23-24] proposed an incremental method with the displacement as the primary unknown. In their method also, the linearized incremental equations are used and the elastic-plastic matrix and the geometry are updated after every increment. They studied the upset forging process by incorporating the friction using the beta-stiffness method [24]. Three dimensional elasto plastic finite element analysis has been done by Pillinger et al. [25] using linearized incremental equations.

Linearized incremental equations give only an approximate solution. If the incremental size is not sufficiently small, the error between the exact and the approximate solutions grows rapidly with the applied load, as the error in the solution of the current increment gets propagated into the next increment when the stress-strain matrix and the geometry are updated. To avoid this phenomenon, the non-linear incremental equations should be solved by using a scheme like Newton-Raphson technique. Such a formulation was first proposed by Bathe et al. [26]. This formulation (with or without elastic effects) has been applied to the forging problem by many researchers. It was applied by Carter and Lee [27] to axisymmetric upsetting. The three dimensional rigid-viscoplastic finite element analysis was done by Park and Kobayashi [28].

Recently Choi et al. [29] developed three dimensional rigid-plastic finite element formulation with special attention to treatment of the contact between the dies and workpiece. At high reduction, a part of the free surface of the workpiece comes in contact with die. This phenomenon has been included in the formulation of Choi et al. [29]. Terziyski et al. [30] used Arbitrary Lagrangian-Eulerian (ALE) FEM for three dimensional forging. Surdon and Chenot [31] developed rigid viscoplastic finite element formulation for hot forging process. It considered thermal effects but didn't use objective stress and strain measures. It neglected elastic effects as the rigid plastic/viscoplastic approach converges in fewer iterations as compared to elastic plastic/viscoplastic approach. Fu and Luo [32] used rigid-viscoplastic finite element formulation for predicting defects in isothermal forging.

The thrust of most of the above studies has been to find an accurate estimation of the forging load, to study the deformation field or to predict fracture. As far as the determination of residual stresses is concerned, there are hardly any attempts [33]. A major difficulty in finding the residual stresses in forging is that the increment size has to be very small in order to achieve a reasonable level of accuracy in the stress values. This leads to a prohibitively large amount of computational time. The Jaumann stress measure, which is the objective stress measure used presently in the literature, does not give accurate stress values if the incremental shear deformation is large. Thus, there is a need to look for a new objective stress measure which will allow the use of a large increment size without compromising on the accuracy of stresses. Such a measure has been recently proposed in reference [34].

1.2 Modelling of Cold Forging Process

In the present work, residual stresses in three dimensional cold upset forging are studied. The updated Lagrangian formulation which is convenient for handling material and geometric nonlinearities is used. New incremental objective stress measure and logarithmic strain measure are used instead of Jaumann stress rate and Green-Lagrange nonlinear strain used in most of the literature. Forging process is a displacement controlled problem. Therefore, to accelerate the convergence of iterative scheme, arc length method is used in conjunction with modified Newton Raphson iterative technique. During unloading, the process can be modelled as a force controlled problem, hence only modified Newton Rapson iterative scheme is used. The material is assumed to be elastic-plastic strain hardening yielding according to von Mises criterion. The effect of temperature and strain rate (viscoplastic effects) on the yield strength of the material are ignored in this work. The inclusion of these effects renders the analysis quite complex. Due to small acceleration, inertial forces are not included. The body forces are also neglected.

The dies are assumed to be rigid and rough. So no relative displacement is permitted at the die-workpiece interface and the process is considered under condition of complete sticking at the die-workpiece interface. The sliding friction at the die-workpiece interface, which applies to the case of smooth lubricated die, is not considered due to lack of time.

1.3 Objective

The objective of the present work is to develop a 3-D large deformation elastoplastic finite element code for determination of residual stresses in cold forging process. The updated Lagrangian formulation is to be used along with new incremental objective stress measure and logarithmic strain measure. The arc length method is to be used in conjunction with the Newton-Raphson technique to solve the non-linear incremental equations of the displacement controlled problem.

First, the code is checked for mesh convergence and then validated by comparing the results with experimental results of reference [28]. Next, a detailed parametric study of residual stresses is carried out to show the effects of three process variables namely the percentage reduction in height, the geometric ratios (height to width ratio, width to thickness ratio) and the material properties. For a typical case, the normal stress distribution at the die-workpiece interface and the deformation patterns after loading and unloading are also presented.

1.4 Plan of The Thesis

The thesis is organized as follows.

In the second chapter, the mathematical modelling of forging process, the 3-D finite element formulation and the numerical scheme are presented. The boundary conditions are discussed at the end of chapter.

In chapter 3, the mesh convergence of the code, the validation and the results for a typical case are presented. It also includes a discussion on the parametric study.

Conclusions and suggestions for further work are presented in chapter 4.

Chapter 2

Mathematical Modelling and Finite Element Formulation of 3-D Forging Process

In this chapter mathematical model and Finite Element formulation of a cold forging process is Developed. The process is modelled as a 3-D problem. The description of motion, stress measures, strain measures and constitutive laws used in the formulation of the governing equation for static large deformation elasto-plastic problems are presented in sections 2.1-2.6 . The finite element formulation and numerical schemes, required to implement the finite element formulation, are presented in sections 2.7-2.9. The boundary conditions for 3-D forging are discussed in section 2.10.

2.1 Updated Lagrangian Formulation

In the study of the deformation of a body subjected to external loading, often the original undeformed and unstressed state of the body is used for the for-

mulation of its equation of motion. This is known as Lagrangian formulation. This formulation is convenient for small deformation which is the case in a majority of engineering problems. In such cases, the deformed configuration does not deviate much from the original one and hence the deformation can be described by an infinitesimal strain tensor, known as the engineering strain tensor, for which the strain-displacement relations are linear. On the other hand, for large deformation problems, one has to use a finite strain measure which is expressed by a nonlinear strain-displacement relation. Furthermore, the equations of motion when expressed in the reference configuration depend on the deformation. Hence, for all large deformation problems, the Lagrangian formulation proves to be cumbersome with the governing equations being difficult to solve. In such cases, one solves the problem using an incremental method known as Updated Lagrangian formulation. In this formulation, it is assumed that the state of the stress and deformation of the body is known till the current configuration, say at time t . The main objective is to determine the incremental deformation and stresses during an infinitesimal time step, Δt , i.e. from time t to $t + \Delta t$. Here, the current configuration is used as the reference configuration for obtaining the incremental values. Unlike in the Lagrangian formulation, an incremental strain tensor is used. This methodology is particularly useful for the elasto-plastic materials because the stress-strain relationship in such materials is usually expressed in an incremental fashion.

2.2 Kinematics of Finite Deformation

The Cartesian co-ordinate x_i of a particle at time τ with reference to the co-ordinate X_j at time t is given by

$$x_i = f_i(X_j, \tau) \quad (2.1)$$

where $t \leq \tau \leq t + \Delta t$.

The relative deformation gradient at time $t + \Delta t$ is defined by ${}^{t+\Delta t}_t F_{ij} = f_{i,j}$ and if ${}^{t+\Delta t}_t \mathbf{F}$ is not singular, the polar decomposition theorem [35] allows a decomposition of the form:

$${}^{t+\Delta t}_t F_{ij} = {}^{t+\Delta t}_t R_{ik} {}^{t+\Delta t}_t U_{kj} \quad (2.2)$$

where ${}^{t+\Delta t}_t \mathbf{R}$ is an orthogonal tensor representing the material rotation and ${}^{t+\Delta t}_t \mathbf{U}$ is a positive definite symmetric tensor called the right stretch tensor. The right stretch tensor can be diagonalized by the following transformation to obtain the principal stretches ${}^{t+\Delta t}_t \lambda_i$:

$${}^{t+\Delta t}_t U_{ij}^P = {}^{t+\Delta t}_t Q_{ik} {}^{t+\Delta t}_t Q_{jl} {}^{t+\Delta t}_t U_{kl} \quad (2.3)$$

where ${}^{t+\Delta t}_t [Q]$ is orthogonal and

$${}^{t+\Delta t}_t \lambda_i = {}^{t+\Delta t}_t U_{ii}^P \quad (\text{no sum}) \quad (2.4)$$

The tensor ${}^{t+\Delta t}_t \mathbf{R}$ and the transformation matrix ${}^{t+\Delta t}_t [Q]$ will be used in the development of a stress measure while the incremental logarithmic strain definition will be obtained from the ${}^{t+\Delta t}_t \lambda_i$.

2.3 Stress Measures

It is essential that an objective stress measure be used in the incremental theory of constitutive modeling to account for the rigid body translation and rotation that may accompany deformation. The Cauchy stress tensor which has great physical significance is not objective and hence cannot be used directly in a constitutive equation. There are numerous objective stress measures and algorithmic formulations (See [36], [37] and the references therein), each with particular advantages and disadvantages. Some of them are discussed below.

The second Piola-Kirchoff stress tensor \mathbf{S} can be related to the Cauchy stress tensor $\boldsymbol{\sigma}$ using the concept of equivalent work between two configurations [38] :

$${}^{t+\Delta t}S_{ij} = \frac{{}^t\rho}{{}^{t+\Delta t}\rho} {}^{t+\Delta t}x_{i,m} {}^{t+\Delta t}\sigma_{mn} {}^tx_{j,n} \quad (2.5)$$

where \mathbf{x} represents position vector and ρ denotes density. The Piola-Kirchoff stress tensor is energy conjugate with the Green-Lagrange strain tensor. This energy conjugate pair is used in the equation for predicting displacements in a predictor-corrector solution procedure (see section 2.7).

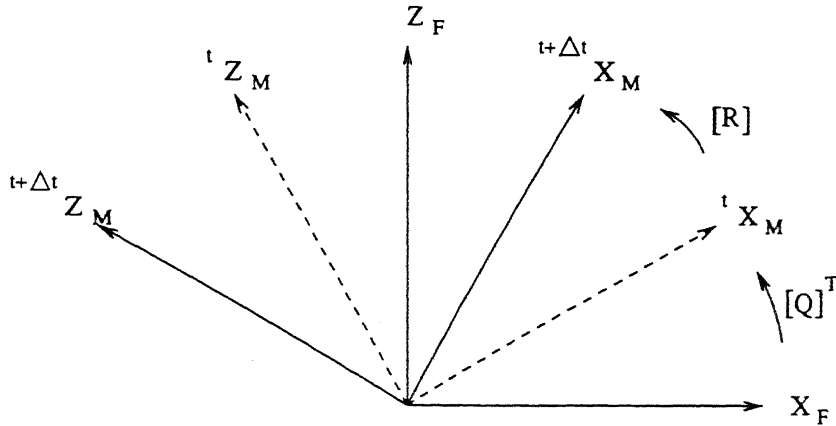
Jaumann discussed the formulation of the rate of change of the stress tensor. The J-rate $\overset{\circ}{\boldsymbol{\sigma}}$ is related to the Cauchy rate $\dot{\boldsymbol{\sigma}}$ by.

$${}^t\overset{\circ}{\sigma}_{ij} \Delta t = {}^t\dot{\sigma}_{ij} \Delta t - {}^t\sigma_{ik} ({}^tW_{jk} \Delta t) - {}^t\sigma_{jk} ({}^tW_{ik} \Delta t) \quad (2.6)$$

where ${}^tW_{ij} \Delta t = \frac{1}{2} ({}_t\Delta u_{i,j} - {}_t\Delta u_{j,i})$ represents the components of the incremental spin tensor. Here, ${}_t\Delta \mathbf{u}$ is the incremental displacement vector.

As pointed out by Metzger and Dubey [39], it is important that the stress

measure used be compatible with the constitutive equation in addition to being objective. An incremental objective stress measure (as against objective stress rate measures) to be used in the generalized Hooke's law and in the elastoplastic constitutive equation is developed below.



The fixed frame is denoted by subscript F
The material frame is denoted by subscript M

Figure 2.1: Fixed and material reference frames

Two Cartesian reference frames (See Figure 2.1) are used :

1. The fixed frame.
2. A material frame which rotates and translates along with a material particle.

The material frame is defined so as to coincide with the principal axes of the right stretch tensor at time t so that the initially orthogonal axes do not get skewed at time $t + \Delta t$.

The first step in the derivation is the transformation of the components of the Cauchy stress tensor at time t from the fixed frame to the material frame:

$${}^t\sigma_{ij}^M = {}^{t+\Delta t}Q_{ik} {}^{t+\Delta t}Q_{jl} {}^t\sigma_{kl} \quad (2.7)$$

The increment in the components of the Cauchy stress tensor with respect to the material axes, ${}_t\Delta\sigma_{ij}^M$, is added to ${}^t\sigma_{ij}^M$ to obtain the stress components at time $t + \Delta t$ with respect to the material frame of reference :

$${}^{t+\Delta t}\sigma_{ij}^M = {}^t\sigma_{ij}^M + {}_t\Delta\sigma_{ij}^M \quad (2.8)$$

The final transformation from the material frame at time $t + \Delta t$ to the fixed frame gives the components of the Cauchy stress tensor at time $t + \Delta t$:

$${}^{t+\Delta t}\sigma_{ij} = {}^{t+\Delta t}Q_{ki} {}^{t+\Delta t}R_{kl} {}^{t+\Delta t}\sigma_{lm}^M {}^{t+\Delta t}R_{nm} {}^{t+\Delta t}Q_{nj} \quad (2.9)$$

The equations (2.7), (2.8) and (2.9) can be combined together to give a relation between the components of the Cauchy stress tensors at times t and $t + \Delta t$ and the increment in the components with respect to the material frame :

$${}^{t+\Delta t}\sigma_{ij} = {}^{t+\Delta t}Q_{ki} {}^{t+\Delta t}R_{kl} \left({}^{t+\Delta t}Q_{lm} {}^t\sigma_{mn} {}^{t+\Delta t}Q_{on} + {}_t\Delta\sigma_{lo}^M \right) {}^{t+\Delta t}R_{po} {}^{t+\Delta t}Q_{pj} \quad (2.10)$$

The proposed stress and the logarithmic strain measures satisfy the requirements of objectivity and lead to a physically consistent application of the usual constitutive equation.

2.4 Strain Measures

The incremental small strain is given by

$${}_t\Delta\epsilon_{ij} = \frac{1}{2}({}_t\Delta u_{i,j} + {}_t\Delta u_{j,i}) \quad (2.11)$$

The incremental Green-Lagrange strain is a non-linear function of the displacement:

$${}_t\Delta e_{ij} = \frac{1}{2}({}_t\Delta u_{i,j} + {}_t\Delta u_{j,i} + {}_t\Delta u_{k,i}{}_t\Delta u_{k,j}) \quad (2.12)$$

These two strain measures occur in the virtual work expression at time $t + \Delta t$ and its transformation to time t respectively. The components of the Green-Lagrange strain tensor are invariant under rigid body rotation of the material unlike the small strain components.

The following are the disadvantages of using one of the above measures in a constitutive law :

1. The solution obtained is dependent upon the size of the increment in the updated Lagrangian formulation unless the increment size is sufficiently small.
2. The components of the strain tensors do not tend to infinite values when the principal stretches tend to zero. Therefore a constitutive law which ensures that the appropriate Cauchy stress components tend to negative infinity (as is physically realistic), even though the strain components remain finite, should be used. This difficulty can be avoided by using a strain measure whose components become minus infinity when the principal stretches become zero.

The logarithmic strain measure introduced by Dienes [36] is free of the above disadvantages. The principal incremental logarithmic strain components, which will be used in this work, are defined by

$${}_t\Delta\epsilon_{ij}^L = \ln({}^{t+\Delta t}{}_t\lambda_i) \delta_{ij} \quad (2.13)$$

where the λ_i are the principal stretches defined by equation (2.4). The logarithmic strain has the following additional advantage in elasto-plastic analysis. A loading test involving elasto-plastic deformation followed by elastic unloading reveals that the slope of the elastic unloading line is the same as that of the initial elastic loading line only when the true stress and the logarithmic strain measures are used in a constitutive law [40].

2.5 Elastic Constitutive Equation

A constitutive law must satisfy the principle of material frame indifference [35]. The elastic constitutive equation used is the generalized Hooke's law relating the increment in stress components with respect to the material frame and the elastic part ($[\Delta\epsilon^{eL}]$) of the principal incremental logarithmic strain components :

$${}_t\Delta\sigma_{ij}^M = \int_t^{t+\Delta t} C_{ijkl}^E d({}_t\Delta\epsilon_{kl}^{eL}) \quad (2.14)$$

The tensor C^E for the isotropic case is given by

$$C_{ijkl}^E = \lambda \delta_{ij} \delta_{kl} + 2\mu \delta_{ik} \delta_{jl} \quad (2.15)$$

where λ and μ are Lamé's constants.

In case anisotropic behavior is modeled, the tensor C^E has to be evaluated with reference to the directions of the principal stretches.

The stress and strain measures used in a constitutive equation need not necessarily be energy conjugate with each other. However if it is so, the predicted response in a predictor-corrector scheme will be closer to the actual response.

2.6 Elasto-plastic Constitutive Equation

As stresses developed in a material exceed the yield stress, the linear relationship between the stress and strain no longer remains valid. We now develop a relationship between the stress and strain based on the von Mises yield criterion and isotropic hardening ¹.

For an isotropically hardening material, the plastic potential is given by [41] :

$$F(\sigma_{ij}, p) = \sigma_{eq}(\sigma_{ij}) - \sigma_y(p) \quad (2.16)$$

Note that

$$F = 0 \quad (2.17)$$

represents the yield criterion. The plastic potential F depends on the Cauchy stress tensor σ_{ij} through it's second invariant σ_{eq} called as equivalent stress and defined by

$$\sigma_{eq} = \left(\frac{3}{2} \sigma'_{ij} \sigma'_{ij} \right)^{\frac{1}{2}} \quad (2.18)$$

¹In this section, the superscript/ subscript denoting time has been omitted for the sake of convenience.

where σ'_{ij} is the deviatoric part of σ_{ij} . Further, F depends on the variable yield stress of the material, σ_y , through a hardening variable p . For the case of strain hardening, p is identified as the equivalent plastic strain ϵ_{eq}^p , and hence defined as :

$$p = \epsilon_{eq}^p = \int d\epsilon_{eq}^p \quad (2.19)$$

and

$$d\epsilon_{eq}^p = \left(\frac{2}{3} d\epsilon_{ij}^p d\epsilon_{ij}^p \right)^{\frac{1}{2}} \quad (2.20)$$

Here, $d\epsilon_{ij}^p$ is the plastic part of the incremental linear strain tensor $d\epsilon_{ij}$ and the integration in equation (2.19) is to be carried along the particle path. The dependence of σ_y on p (or ϵ_{eq}^p) is normally approximated by a power-law type of relationship

$$\sigma_y - (\sigma_y)_0 = K(\epsilon_{eq}^p)^n \quad (2.21)$$

Here, $(\sigma_y)_0$ is the yield stress at zero plastic strain, K is called the hardening coefficient and n is called as the hardening exponent.

The plastic part of incremental linear strain tensor ($d\epsilon_{ij}^p$) is obtained from the plastic potential using the following relation :

$$d\epsilon_{ij}^p = d\lambda \frac{\partial F}{\partial \sigma_{ij}} \quad (2.22)$$

where $d\lambda$ is a scalar. This equation is called as the flow rule. Differentiation of equation 2.16 with respect to σ_{ij} gives

$$\frac{\partial F}{\partial \sigma_{ij}} = \frac{3}{2\sigma_{eq}} \sigma'_{ij} \quad (2.23)$$

Using this, one can determine $d\lambda$ as :

$$d\lambda = d\epsilon_{eq}^p \quad (2.24)$$

Further, the hardening relationship and the yield condition can be used to express $d\lambda$ as :

$$d\lambda = \frac{d\sigma_y}{H} = \frac{d\sigma_{eq}}{H} \quad (2.25)$$

where

$$H = \frac{d\sigma_y}{d\epsilon_{eq}^p} = K n (\epsilon_{eq}^p)^{n-1} \quad (2.26)$$

is the slope of the hardening curve. Substitution of equations (2.23) and (2.25) in equation (2.22) leads to the following constitutive equation

$$d\epsilon_{ij}^p = \frac{3}{2} \frac{d\sigma_{eq}}{H \sigma_{eq}} \sigma'_{ij} \quad (2.27)$$

This constitutive relationship between the deviatoric stress tensor and the plastic part of incremental linear strain tensor is not really convenient for the Updated Lagrangian formulation for which the incremental stress-strain relationship is needed. This can be obtained from equation (2.27) as follows :

$$d\epsilon_{ij}^p = \frac{3}{2} \frac{\sigma'_{ij}}{H \sigma_{eq}} \frac{\partial \sigma_{eq}}{\partial \sigma_{kl}} d\sigma_{kl} \quad (2.28)$$

Note that, from equations (2.16) and (2.23), we get

$$\frac{\partial \sigma_{eq}}{\partial \sigma_{kl}} = \frac{\partial F}{\partial \sigma_{kl}} = \frac{3}{2 \sigma_{eq}} \sigma'_{kl} \quad (2.29)$$

Substitution of equation (2.29) in equation (2.28) leads to the following incremental plastic stress-strain relationship :

$$d\epsilon_{ij}^p = \frac{9 \sigma'_{ij} \sigma'_{kl}}{4 H \sigma_{eq}^2} d\sigma_{kl}. \quad (2.30)$$

The incremental elastic stress strain relationship (equations 2.14-2.15) can now be written as

$$d\epsilon_{ij}^e = \frac{1}{E} [-\nu d\sigma_{kk} \delta_{ij} + (1 + \nu) d\sigma_{ij}] \quad (2.31)$$

where $d\epsilon_{ij}^e$ is the elastic part of $d\epsilon_{ij}$, E is the Young's modulus and ν is the Poisson's ratio. Adding the two relationships, we get

$$d\epsilon_{ij} = d\epsilon_{ij}^e + d\epsilon_{ij}^p \quad (2.32)$$

$$= \left[-\frac{\nu}{E} \delta_{ij} \delta_{kl} + \frac{(1+\nu)}{E} \delta_{ik} \delta_{jl} + \frac{9\sigma'_{ij} \sigma'_{kl}}{4H\sigma_{eq}^2} \right] d\sigma_{kl} \quad (2.33)$$

This is the incremental elasto-plastic stress-strain relationship needed in the Updated Lagrangian formulation. However, it is the following inverse relationship which is more useful :

$$d\sigma_{ij} = C_{ijkl}^{EP} d\epsilon_{kl} \quad (2.34)$$

where

$$C_{ijkl}^{EP} = 2\mu \left[\delta_{ik} \delta_{jl} + \frac{\nu}{1-2\nu} \delta_{ij} \delta_{kl} - \frac{9\mu \sigma'_{ij} \sigma'_{kl}}{2(3\mu + H) \sigma_{eq}^2} \right] \quad (2.35)$$

and μ is one of the Lamé's constant (also called as shear modulus) appearing in eq. (2.15).

Note that the stress increment appearing in eq. (2.34) must be an objective stress increment in the sense that $d\sigma_{ij}$ must reduce to a zero tensor in the event of the increment being a pure rigid rotation. The incremental objective stress measure to be used in the present work has been described in section 2.3 .

The relationship (2.34) has been derived assuming the increment size to be small and using the incremental linear strain tensor as the strain measure. When a large-size increment is to be used along with the incremental logarithmic strain measure (defined in section 2.4), the derivation is similar. The relationship (2.34), when the stress and strain measures are replaced respectively by the incremental objective stress measure (of section 2.3) and the

incremental logarithmic strain measure (of section 2.4), takes the following form with respect to the material frame :

$${}^t\Delta\sigma_{ij}^M = \int_t^{t+\Delta t} {}^tC_{ijkl}^{EP} d({}^t\Delta\epsilon_{kl}^L) \quad (2.36)$$

where

$${}^tC_{ijkl}^{EP} = 2\mu \left[\delta_{ik}\delta_{jl} + \frac{\nu}{1-2\nu}\delta_{ij}\delta_{kl} - \frac{9\mu {}^t\sigma'_{ij} {}^t\sigma'_{ij}}{2(3\mu + Kn({}^t\epsilon_{eq}^p)^{n-1}) {}^t\sigma_{eq}^2} \right] \quad (2.37)$$

Here, H has been replaced by the expression (2.26) and the left superscript t has been added to make it explicit that these quantities are to be evaluated at that time.

2.7 Incremental Updated Lagrangian Formulation

The objective of the updated Lagrangian formulation is to establish static equilibrium in the configuration at time $t + \Delta t$ when all static variables at time t are known.

The principle of virtual work requires that

$$\int_{t+\Delta t V} {}^{t+\Delta t}\sigma_{ij} \delta({}^{t+\Delta t}\epsilon_{ij}) d{}^{t+\Delta t}V = {}^{t+\Delta t}R \quad (2.38)$$

where

${}^{t+\Delta t}\sigma_{ij}$ = Cartesian component of the Cauchy stress tensor at time $t + \Delta t$

$$\delta {}^{t+\Delta t}\epsilon_{ij} = \frac{1}{2} \left(\frac{\partial \delta {}^{t+\Delta t}u_i}{\partial {}^{t+\Delta t}x_j} + \frac{\partial \delta {}^{t+\Delta t}u_j}{\partial {}^{t+\Delta t}x_i} \right)$$

$\delta {}^{t+\Delta t}u_i$ = Cartesian component of the virtual displacement at time $t + \Delta t$

${}^{t+\Delta t}x_i$ = Cartesian co-ordinate of a material point at time $t + \Delta t$

${}^{t+\Delta t}V$ = Volume at time $t + \Delta t$

and

$${}^{t+\Delta t}R = \int_{{}^{t+\Delta t}S_f} {}^{t+\Delta t}f_i^S \delta {}^{t+\Delta t}u_i d{}^{t+\Delta t}S \quad (2.39)$$

where

${}^{t+\Delta t}f_i^S$ = Cartesian component of external traction per unit area at time $t + \Delta t$

${}^{t+\Delta t}S_f$ = Surface at time $t + \Delta t$ with traction specified

The main difficulty in the application of equation (2.38) is that the configuration at time $t + \Delta t$ is unknown. An elegant way of formulating the problem is given by Bathe [42]. The virtual work expression at time $t + \Delta t$ is transformed to an integral over the volume at time t by using the second Piola-Kirchoff stress and Green-Lagrange strain measures, which are energy conjugate to each other, and the principle of conservation of mass. It is assumed that the external load term (2.39) is deformation independent for the formulation of the governing equation. The expression (2.38) after the transformation becomes

$$\int_{{}^tV} {}^{t+\Delta t}{}_tS_{ij} \delta ({}^{t+\Delta t}{}_te_{ij}) d{}^tV = {}^{t+\Delta t}R \quad (2.40)$$

The Green-Lagrange strain tensor ${}^{t+\Delta t}{}_te$ is defined by

$${}^{t+\Delta t}{}_te_{ij} = \frac{1}{2} \left({}^{t+\Delta t}{}_tu_{i,j} + {}^{t+\Delta t}{}_tu_{j,i} + {}^{t+\Delta t}{}_tu_{k,i} {}^{t+\Delta t}{}_tu_{k,j} \right) \quad (2.41)$$

The following quantities are incrementally decomposed :

$$\begin{aligned} {}^{t+\Delta t}{}_tS_{ij} &= {}^tS_{ij} + {}_t\Delta S_{ij} \\ &= {}^t\sigma_{ij} + {}_t\Delta S_{ij} \end{aligned} \quad (2.42)$$

$$\delta(^{t+\Delta t}u_i) = \delta(^tu_i + {}_t\Delta u_i) = \delta({}_t\Delta u_i) \quad (2.43)$$

$$\begin{aligned} \delta(^{t+\Delta t}e_{ij}) &= \delta({}_t\Delta e_{ij}) \\ &= \delta({}_t\Delta \epsilon_{ij} + {}_t\Delta \eta_{ij}) \end{aligned} \quad (2.44)$$

where

$${}_t\Delta \epsilon_{ij} = \frac{1}{2} ({}_t\Delta u_{i,j} + {}_t\Delta u_{j,i}) \quad (2.45)$$

$${}_t\Delta \eta_{ij} = \frac{1}{2} {}_t\Delta u_{k,i} {}_t\Delta u_{k,j} \quad (2.46)$$

Therefore equation (2.40) can be written with incremental decomposition as

$$\begin{aligned} &\int_{tV} {}_t\Delta S_{ij} \delta({}_t\Delta \epsilon_{ij}) d^tV + \int_{tV} {}_t\Delta S_{ij} \delta({}_t\Delta \eta_{ij}) d^tV \\ &+ \int_{tV} {}^t\sigma_{ij} \delta({}_t\Delta \eta_{ij}) d^tV + \int_{tV} {}^t\sigma_{ij} \delta({}_t\Delta \epsilon_{ij}) d^tV = {}^{t+\Delta t}R \end{aligned} \quad (2.47)$$

The above equation is linearized by neglecting the second integral which is a higher order term and approximating ${}_t\Delta S_{ij}$ as ${}^tC_{ijkl}^{EP} {}_t\Delta \epsilon_{kl}$:

$$\begin{aligned} &\int_{tV} {}^tC_{ijkl}^{EP} {}_t\Delta \epsilon_{kl} \delta({}_t\Delta \epsilon_{ij}) d^tV + \int_{tV} {}^t\sigma_{ij} \delta({}_t\Delta \eta_{ij}) d^tV \\ &+ \int_{tV} {}^t\sigma_{ij} \delta({}_t\Delta \epsilon_{ij}) d^tV = {}^{t+\Delta t}R \end{aligned} \quad (2.48)$$

The linearized equation, when solved, will yield only approximate displacement, strain and stress fields. The approximate quantities are denoted by a right superscript (1). The error due to the approximation involved is calculated from equation (2.38) as

$$Error = {}^{t+\Delta t}R - \int_{t+\Delta tV^{(1)}} {}^{t+\Delta t}\sigma_{ij}^{(1)} \delta(^{t+\Delta t}\epsilon_{ij}^{(1)}) d^{t+\Delta t}V^{(1)} \quad (2.49)$$

This error is generally minimized by a predictor-corrector scheme. The next section discusses the techniques used for obtaining the solution to the governing equation (2.47).

2.8 Finite Element Formulation

A finite element method for solving the linearized equation and an iterative numerical technique for minimizing the error is described in this section.

2.8.1 Matrix Notation

Matrix notation is used in the development of the finite element equations for the convenience of computer implementation.

The components of the tensors ${}_t\Delta\epsilon$, ${}_t\Delta\eta$ and ${}_t\Delta\epsilon^L$ are represented in array form as follows:

$${}_t\{\Delta\epsilon\}^T = \{{}_t\Delta\epsilon_{xx}, {}_t\Delta\epsilon_{yy}, {}_t\Delta\epsilon_{zz}, 2{}_t\Delta\epsilon_{xy}, 2{}_t\Delta\epsilon_{yz}, 2{}_t\Delta\epsilon_{xz}\} \quad (2.50)$$

$${}_t\{\Delta\eta\}^T = \{{}_t\Delta u_{,x}, {}_t\Delta u_{,y}, {}_t\Delta u_{,z}, {}_t\Delta v_{,x}, {}_t\Delta v_{,y}, \dots\} \quad (2.51)$$

$${}_t\{\Delta\epsilon^L\}^T = \{{}_t\Delta\epsilon_{xx}^L, {}_t\Delta\epsilon_{yy}^L, {}_t\Delta\epsilon_{zz}^L, {}_t\Delta\epsilon_{xy}^L, {}_t\Delta\epsilon_{yz}^L, {}_t\Delta\epsilon_{xz}^L\} \quad (2.52)$$

The components of all stress tensors are written as arrays with respective components placed in the following manner:

$$\{\sigma\}^T = \{\sigma_{xx}, \sigma_{yy}, \sigma_{zz}, \sigma_{xy}, \sigma_{yz}, \sigma_{zx}\} \quad (2.53)$$

Two matrix forms of the tensor ${}^tC_{ijkl}^{EP}$ (given by eq. 2.37) are needed:

1. ${}^t[C^{EP}]'$ for the constitutive relationship ${}_t\{\Delta S\} = {}^t[C^{EP}]'{}_t\{\Delta\epsilon\}$
2. ${}^t[C^{EP}]$ for the constitutive relationship ${}_t\{\Delta\sigma^M\} = {}^t[C^{EP}]{}_t\{\Delta\epsilon^L\}$

They are given by

$${}^t[C^{EP}]' = \left([C^{E'}] - \frac{[C^{E'}] {}^t\{a\} {}^t\{a\}^T [C^{E'}]}{{}^tH + {}^t\{a\}^T [C^{E'}] {}^t\{a\}} \right) \quad (2.54)$$

$${}^t[C^{EP}] = \left([C^E] - \frac{[C^E] {}^t\{a\} {}^t\{a\}^T [C^E]}{{}^tH + {}^t\{a\}^T [C^E] {}^t\{a\}} \right) \quad (2.55)$$

In the above equations,

$${}^t\{a\} = \frac{3}{2 {}^t\sigma_{eq}} {}^t\{\sigma'\} \quad (2.56)$$

and the array ${}^t\{\sigma'\}$ represents the deviatoric part of the Cauchy stress at time t . For an isotropic material, the matrices $[C^{E'}]$ and $[C^E]$ for the 3-D case are given by

$$[C^{E'}] = \frac{E}{(1+\nu)(1-2\nu)} \begin{bmatrix} 1-\nu & \nu & \nu & 0 & 0 & 0 \\ \nu & 1-\nu & \nu & 0 & 0 & 0 \\ \nu & \nu & 1-\nu & 0 & 0 & 0 \\ 0 & 0 & 0 & \frac{1-2\nu}{2} & 0 & 0 \\ 0 & 0 & 0 & 0 & \frac{1-2\nu}{2} & 0 \\ 0 & 0 & 0 & 0 & 0 & \frac{1-2\nu}{2} \end{bmatrix} \quad (2.57)$$

$$[C^E] = \frac{E}{(1+\nu)(1-2\nu)} \begin{bmatrix} 1-\nu & \nu & \nu & 0 & 0 & 0 \\ \nu & 1-\nu & \nu & 0 & 0 & 0 \\ \nu & \nu & 1-\nu & 0 & 0 & 0 \\ 0 & 0 & 0 & 1-2\nu & 0 & 0 \\ 0 & 0 & 0 & 0 & 1-2\nu & 0 \\ 0 & 0 & 0 & 0 & 0 & 1-2\nu \end{bmatrix} \quad (2.58)$$

Equation (2.48) can be written in the following form owing to the symmetries in ${}^tC^{EP}$, ${}^t\Delta\epsilon$, ${}^t\Delta\eta$ and ${}^t\sigma$:

$$\begin{aligned} \int_{tV} \delta({}^t\{\Delta\epsilon\}^T) {}^t[C^{EP}] {}^t\{\Delta\epsilon\} d^tV + \int_{tV} \delta({}^t\{\Delta\eta\}^T) {}^t[T] {}^t\{\Delta\eta\} d^tV \\ + \int_{tV} \delta({}^t\{\Delta\epsilon\}^T) {}^t\{\sigma\} d^tV = {}^{t+\Delta t}R \end{aligned} \quad (2.59)$$

The matrix ${}^t[T]$ is given by:

$${}^t[T] = \begin{bmatrix} {}^t[\Sigma] & 0 & 0 \\ 0 & {}^t[\Sigma] & 0 \\ 0 & 0 & {}^t[\Sigma] \end{bmatrix} \quad (2.60)$$

where

$${}^t[\Sigma] = \begin{bmatrix} {}^t\sigma_{xx} & {}^t\sigma_{xy} & {}^t\sigma_{zx} \\ {}^t\sigma_{xy} & {}^t\sigma_{yy} & {}^t\sigma_{yz} \\ {}^t\sigma_{zx} & {}^t\sigma_{yz} & {}^t\sigma_{zz} \end{bmatrix} \quad (2.61)$$

2.8.2 Finite Element Equation

The domain is discretized into a number of elements and the incremental displacement field is approximated over each element by

$${}_t\{\Delta u\} = \begin{Bmatrix} {}_t\Delta u \\ {}_t\Delta v \\ {}_t\Delta w \end{Bmatrix} = {}^t[\Phi] {}_t\{\Delta u\}^e \quad (2.62)$$

where the element incremental displacement vector ${}_t\{\Delta u\}^e$ is given by

$${}_t\{\Delta u\}^e = \{ {}_t\Delta u^1, {}_t\Delta v^1, {}_t\Delta w^1, {}_t\Delta u^2, {}_t\Delta v^2, {}_t\Delta w^2, \dots \} \quad (2.63)$$

The quantities ${}_t\Delta u^i, {}_t\Delta v^i, {}_t\Delta w^i$ stand for the unknown incremental displacements of node i in X, Y and Z directions respectively and the matrix ${}^t[\Phi]$ is defined by

$${}^t[\Phi] = \begin{bmatrix} {}^t\{\Phi_1\}^T \\ {}^t\{\Phi_2\}^T \\ {}^t\{\Phi_3\}^T \end{bmatrix} \quad (2.64)$$

where

$$\begin{aligned} {}^t\{\Phi_1\}^T &= \{ {}^tN_1, 0, 0, {}^tN_2, 0, 0, {}^tN_3, \dots \}, \\ {}^t\{\Phi_2\}^T &= \{ 0, {}^tN_1, 0, 0, {}^tN_2, 0, 0, \dots \}, \\ {}^t\{\Phi_3\}^T &= \{ 0, 0, {}^tN_1, 0, 0, {}^tN_2, 0, \dots \} \end{aligned} \quad (2.65)$$

The tN_i , which are functions of $({}^tx, {}^ty, {}^tz)$, are called shape functions and are determined by the element used. The 8-noded brick element with linear shape functions [43] is used in this work.

The strain field is expressed in terms of the nodal displacements by differentiating (2.62) and using the expressions (2.45) and (2.46) as

$${}^t\{\Delta\epsilon\} = {}^t[B_L] {}^t\{\Delta u\}^e \quad (2.66)$$

$${}^t\{\Delta\eta\} = {}^t[B_N] {}^t\{\Delta u\}^e \quad (2.67)$$

where

$${}^t[B_L] = \begin{bmatrix} {}^t\{\Phi_1\}_{,x}^T \\ {}^t\{\Phi_2\}_{,x}^T \\ {}^t\{\Phi_3\}_{,x}^T \\ {}^t\{\Phi_1\}_{,y}^T + {}^t\{\Phi_2\}_{,z}^T \\ {}^t\{\Phi_3\}_{,y}^T + {}^t\{\Phi_1\}_{,z}^T \\ {}^t\{\Phi_2\}_{,z}^T + {}^t\{\Phi_3\}_{,x}^T \end{bmatrix} \quad (2.68)$$

and

$${}^t[B_N]^T = [{}^t\{\Phi_1\}_{,x}, {}^t\{\Phi_1\}_{,y}, {}^t\{\Phi_1\}_{,z}, {}^t\{\Phi_2\}_{,x}, {}^t\{\Phi_2\}_{,y}, \dots] \quad (2.69)$$

Using equations (2.62), (2.66) and (2.67), the contribution to the integral (2.59) over a typical element e with volume V^e is

$$\begin{aligned} & \delta ({}^t\{\Delta u\}^{eT}) \left(\int_{V^e} {}^t[B_L]^T {}^t[C^{EP'}] {}^t[B_L] d^tV^e \right) {}^t\{\Delta u\}^e + \\ & \delta ({}^t\{\Delta u\}^{eT}) \left(\int_{V^e} {}^t[B_N]^T {}^t[T] {}^t[B_N] d^tV^e \right) {}^t\{\Delta u\}^e + \\ & \delta ({}^t\{\Delta u\}^{eT}) \left(\int_{V^e} {}^t[B_L]^T {}^t\{\sigma\} d^tV^e \right) = \delta ({}^t\{\Delta u\}^{eT}) {}^{t+\Delta t}\{F\}^e \end{aligned} \quad (2.70)$$

The contribution to the term ${}^{t+\Delta t}R$ is expressed in terms of the elemental external force vector ${}^{t+\Delta t}\{F\}^e$ using a standard procedure [43]. Since the

variation in the displacement vector is arbitrary, the above equation can be written as

$${}^t[K]^e {}_t\{\Delta u\}^e + {}^t\{f\}^e = {}^{t+\Delta t}\{F\}^e \quad (2.71)$$

The elemental stiffness matrix ${}^t[K]^e$ is expressed as

$${}^t[K]^e = {}^t[K_L]^e + {}^t[K_{NL}]^e \quad (2.72)$$

$${}^t[K_L]^e = \int_{tV^e} {}^t[B_L]^T {}^t[C^{EP}] {}^t[B_L] d^tV^e \quad (2.73)$$

$${}^t[K_{NL}]^e = \int_{tV^e} {}^t[B_N]^T {}^t[T] {}^t[B_N] d^tV^e \quad (2.74)$$

The elemental internal force vector is

$${}^t\{f\}^e = \int_{tV^e} {}^t[B_L]^T {}^t\{\sigma\} d^tV^e \quad (2.75)$$

The elemental stiffness matrices ${}^t[K]^e$ along with the elemental force vectors ${}^t\{f\}^e$ and ${}^{t+\Delta t}\{F\}^e$ are assembled to obtain the global equation :

$${}^t[K] {}_t\{\Delta u\} + {}^t\{f\} = {}^{t+\Delta t}\{F\} \quad (2.76)$$

Decomposing ${}^{t+\Delta t}\{F\}$, eqn. (2.76) can be written as

$${}^t[K] {}_t\{\Delta u\} + {}^t\{f\} = {}^t\{F\} + {}_t\{\Delta F\} \quad (2.77)$$

Here, ${}^t\{F\}$ is the (global) external force vector at time t and ${}_t\{\Delta F\}$ is the (global) incremental force vector from time t to $t+\Delta t$. In Updated Lagrangian formulation, it is assumed that the equilibrium equations are satisfied exactly at time t . Thus

$${}^t\{f\} = {}^t\{F\} \quad (2.78)$$

Then eqn (2.77) reduces to

$${}^t[K] {}_t\{\Delta u\} = {}_t\{\Delta F\} \quad (2.79)$$

This equation is solved to obtain the incremental displacement vector ${}_t\{\Delta u\}$. The wavefront equation solver as described by Irons and Ahmad [44], has been implemented with buffer and blocking concepts to solve large systems of equations. A resolving facility, whose need will become apparent later, is also present.

2.8.3 Determination of Stresses

The evaluation of the stress components (at the Gauss points of the elements) is done by the following stepwise procedure :

1. Calculate the relative deformation gradient ${}^{t+\Delta t}{}_t[F]$

$${}^{t+\Delta t}{}_tF_{ij} = \delta_{ij} + \frac{\partial({}_t\Delta u_i)}{\partial x_j} \quad (2.80)$$

It should be noted that the position vector ${}^t\mathbf{x}$ corresponds to the equilibrium position.

2. Decompose ${}^{t+\Delta t}{}_t[F] = {}^{t+\Delta t}{}_t[R] {}^{t+\Delta t}{}_t[U]$ and determine ${}^{t+\Delta t}{}_t[Q]$ and ${}^{t+\Delta t}{}_t[U^P]$ using equation (2.3).
3. Determine the principal incremental logarithmic strain ${}_t\{\Delta \epsilon^L\}$ using equation (2.13).
4. Calculate ${}_t\{\Delta \sigma^M\}$ using equation (2.36). The integration of the constitutive equation is performed using the Euler forward technique described below.
5. Use equation (2.10) to calculate the Cauchy stress components at time $t + \Delta t$.

2.8.4 Integration of the Constitutive Equation

Different techniques exist for the integration of the constitutive equation [38]. A simple and robust technique is the Euler forward integration scheme described below.

Assume that the principal incremental strain components have been calculated and the state of the Gauss point at time t (*elastic or plastic*) is known.

- If the state at time t is *elastic*,

1. Calculate the stress increment assuming elastic behaviour

$${}_t\{\Delta\sigma^M\} = [C^E]{}_t\{\Delta\epsilon^L\}$$

2. Calculate ${}^{t+\Delta t}\{\sigma\}$ using (2.10)

3. Determine ${}^t\sigma_{eq}$ and ${}^{t+\Delta t}\sigma_{eq}$ using (2.18)

4. If ${}^{t+\Delta t}\sigma_{eq} \leq {}^{t+\Delta t}\sigma_y$ then elastic behaviour holds, or if ${}^{t+\Delta t}\sigma_{eq} = {}^t\sigma_{eq}$ the Gauss point is neutrally loaded. **Return.**

5. If ${}^{t+\Delta t}\sigma_{eq} > {}^{t+\Delta t}\sigma_y$ a transition from elastic to plastic state has occurred. Calculate

$$Ratio = \frac{({}^{t+\Delta t}\sigma_y - {}^t\sigma_{eq})}{({}^{t+\Delta t}\sigma_{eq} - {}^t\sigma_{eq})}$$

and change the state to *plastic*. The sub-incrementation method is followed and the stress tensor components with respect to the material frame are updated for each sub increment by the increment

in stress components corresponding to the elasto-plastic strain sub-increment. The $[C^{EP}]$ corresponding to last updated state is used:

$${}^{t+\Delta t}\{\sigma^M\}^{(i)} = {}^{t+\Delta t}\{\sigma^M\}^{(i-1)} + {}^{t+\Delta t}[C^{EP}]^{(i-1)} d_t\{\Delta\epsilon^L\} \quad \text{for } i = 1, n$$

where

$$\begin{aligned} d_t\{\Delta\epsilon^L\} &= \frac{(1 - Ratio)_t\{\Delta\epsilon^L\}}{n} \\ {}^{t+\Delta t}\{\sigma^M\}^{(0)} &= {}^t\sigma^M + Ratio[C^E]_t\{\Delta\epsilon^L\} \\ {}^{t+\Delta t}[C^{EP}]^{(0)} &= [C^{EP}] \text{ evaluated at } {}^{t+\Delta t}\{\sigma^M\}^{(0)} \end{aligned}$$

Use equation (2.10) to find ${}^{t+\Delta t}\sigma_{ij}$. **Return.**

- If the state at time t is *plastic*, the sub incrementation method described in (5) above is applied with *Ratio* set to zero.

This describes the Euler forward scheme for the elasto-plastic model described in section 2.6 .

2.8.5 Unloading Scheme

The phenomenon of local unloading has to be incorporated to reproduce more closely the elasto-plastic response of the structure. The unloading criterion defined by Chakrabarty [45] is implemented:

$${}^t\{n\}^T {}^t\{\Delta\epsilon^L\} < 0 \quad (2.81)$$

where ${}^t\{\Delta\epsilon^L\}$ is the incremental strain and ${}^t\{n\}$ represents the unit outward normal to the yield surface at the current stress point ${}^t\sigma$ in a $9-D$ space. Neutral loading and positive loading are represented by replacing the "less than" symbol in (2.81) by the "equal to" and "greater than" symbols respectively.

When unloading is detected, the yield stress at that Gauss point is changed to the equivalent stress at the Gauss point at time t (${}^t\sigma_y = {}^t\sigma_{eq}$), the state tag of the Gauss point is changed from *plastic* to *elastic* and the elastic constitutive equation is applied to calculate $[\Delta\sigma^M]$.

2.9 Numerical Scheme

2.9.1 Modified Newton-Raphson Scheme

The solution to equation (2.79) represents only an approximate equilibrium equation at time $t + \Delta t$ (the approximation is mostly due to the linearization and simplification involved in the steps between eqn (2.47) to (2.48)). A solution of such an approximate equation may involve a significant amount of error and, depending on incremental displacement step, may become unstable. Therefore, it is necessary to modify eqn (2.79) to turn it into an iterative problem capable of providing a solution with desirable accuracy. There are various iterative techniques for this [38]. The simplest, and for many practical applications effective technique is the modified Newton-Raphson algorithm which offers fast convergence with less computation.

This technique can elegantly be represented as follows:

Solve

$${}^t[K] {}_t\{\Delta u\}^{(i)} = {}_t\{R\}^{(i-1)} \quad (2.82)$$

where

$${}_t\{R\}^{(i-1)} = {}^{t+\Delta t}\{F\}^{(i-1)} - {}^{t+\Delta t}\{f\}^{(i-1)} \quad (2.83)$$

$${}_t\{R\}^{(0)} = {}_t\{\Delta F\} \quad (2.84)$$

till the convergence criterion

$$\frac{\|{}_t\{R\}^{(i)}\|}{\|{}^{t+\Delta t}\{F\}^{(i)}\|} \leq tol_c \quad (2.85)$$

is satisfied. The vector ${}_t\{R\}$ is called as the unbalanced force vector. The right superscript on ${}^{t+\Delta t}\{F\}$ denotes the configuration on which the integration is performed to find the external force vector.

2.9.2 Arc Length Method

Forging problem is a displacement controlled problem i.e. the deformation is controlled by a specified displacement (at the workpiece-die interface) rather than by a specified traction. Since there is no known external force, the denominator in the convergence criterion (2.85) doesn't exist. In that case, one can try to achieve the convergence by making the unbalanced force vector ${}_t\{R\}^{(i)}$ small in an absolute sense. But this slows down the rate of convergence to a considerable extent. To accelerate the rate of convergence, the arc length method is used in conjunction with the modified Newton-Raphson method. In this approach, the unknown nodal reactions at the interface are expressed as a linear combination of a set of known nodal forces. Then the problem is solved as a force controlled problem using the set of known nodal forces. The unknown coefficients in the linear combination are found from the condition that the vertical component of the incremental displacement vector at the interface has a specified value. Since this solution may not satisfy the nodal equilibrium of internal and external forces, iterations need to be performed which are

carried out by the modified Newton-Raphson method. Since both the nodal reactions as well as the unbalance force vector change during an iteration, the incremental equations contain an additional term compared to eq. (2.82).

Originally, the arc length method was proposed only for the case of proportional loading [46, 47]. However, in forging problem, the loading is non-proportional. Therefore, the method needs to be modified appropriately to take care of non-proportional loading. The modified method is described in this section.

In i th iteration, the incremental eq. (2.77) is expressed as ²

$$[K] \{\Delta u\}^{(i)} = \{\Delta F\}^{(i)} + \{R\}^{(i-1)} \quad (2.86)$$

where $\{R\}^{(i-1)}$ is the unbalanced force vector given by

$$\{R\}^{(i-1)} = \{F\}^{i-1} - \{f\}^{i-1} \quad (2.87)$$

and the incremental force vector $\{\Delta F\}^{(i)}$ is expressed as

$$\{\Delta F\}^{(i)} = \sum_{k=1}^m (\Delta \lambda)_k^i \{P\}_k \quad (2.88)$$

Here, m is the number of nodes at the interface and $\{P\}_k$ is a known nodal force vector corresponding to a unit (vertically downward) point force at node k . The vectors $\{P\}_k$, $k = 1, m$ are called as the basic load vectors. The coefficients $(\Delta \lambda)_k^{(i)}$ are unknowns.

Since eq. (2.86) is a linear equation, one can decompose the solution as

$$\{\Delta u\}^{(i)} = \sum_{k=1}^m (\Delta \lambda)_k^{(i)} \{\Delta u^{(k)I}\} + \{\Delta u^{II}\}^{(i)} \quad (2.89)$$

²In this section, the superscript/ subscript denoting time has been omitted for the sake of convenience.

where $\{\Delta u^{(k)I}\}$ and $\{\Delta u^{II}\}^{(i)}$ are obtained as solutions of the following problems :

$$[K] \{\Delta u^{(k)I}\} = \{P\}_k, \quad k = 1, m \quad (2.90)$$

$$[K] \{\Delta u^{II}\}^{(i)} = \{R\}^{(i-1)} \quad (2.91)$$

Thus, $\{\Delta u^{(k)I}\}$ represents the iterative displacement vector due to the basic load vector at node k and $\{\Delta u^{II}\}^{(i)}$ represents the iterative displacement vector due to the unbalanced force vector $\{R\}^{(i-1)}$.

To find the complete solution of eq. (2.86), one needs to determine $(\Delta \lambda)_k^{(i)}$, $k = 1, m$. They are determined from the following condition. At the nodes on the interface, the vertical or z-component of the incremental displacement is known. Thus, for nodes $l = 1, m$:

$$\sum_{k=1}^m (\Delta \lambda)_k^{(i)} \Delta u_{lz}^{(k)I} + \Delta u_{lz}^{II(i)} = \text{specified value} \quad (2.92)$$

These are m equations in m unknowns : $(\Delta \lambda)_k^{(i)}$, $k = 1, m$. By solving these equations, the unknown $\Delta \lambda_k^{(i)}$ are calculated. Then the iterative displacements are determined from eq. (2.89). These displacements are used to find the internal force vector $\{f\}^{(i)}$. Finally, the external force vector at the end (of i th) iteration is found from

$$\{F\}^{(i)} = \{F\}^{(i-1)} + \sum_{k=1}^m \Delta \lambda_k^{(i)} \{P\}_k \quad (2.93)$$

This force vector is used to find the unbalanced force vector and then to check the convergence using eq. (2.85).

While solving eqs. (2.90-2.91), the upper triangularisation of the coefficient matrix $[K]$ needs to be done only once. Then, one can use the resolving

facility first to perform the Gauss elimination operations on different right side vectors and then to find $\{\Delta u^{(k)I}\}$ and $\{\Delta u^{II}\}^{(i)}$ by back substitution.

Equation (2.92) takes a different form for the first iteration than for other iterations. These forms are as follows :

First iteration :

For the first iteration, $\{R\}^{(0)} = \{0\}$ implies that $\{\Delta u^{II}\}^{(1)} = \{0\}$. Thus, eq. (2.92) becomes

$$\sum_{k=1}^m (\Delta \lambda)_k^{(1)} \Delta u_{Iz}^{(k)I} = \text{specified value} \quad (2.94)$$

Subsequent iterations :

Since the value of specified incremental displacement does not change during an iteration cycle, in subsequent iterations, the right side of eq. (2.92) becomes zero. Thus,

$$\sum_{k=1}^m (\Delta \lambda)_k^{(i)} \Delta u_{Iz}^{(k)I} + \Delta u_{Iz}^{II(i)} = 0 \quad i \geq 2 \quad (2.95)$$

2.9.3 Numerical Integration Scheme

Exact evaluation of integrals appearing in element coefficient matrices and right side vectors is not always possible because of the complexity of the integrands. In such cases, it is natural to seek numerical evaluation of these integral expressions. Numerical integration, involves approximation of the integrand by a polynomial of sufficient degree, because the integral of a polynomial can be evaluated exactly.

The most used numerical integration method is Gauss-Legendre numerical integration method. The expression for the integral over a (3-D) Cubic master element Ω_R is given by

$$\begin{aligned} \int_{\Omega_R} F(\xi, \eta, \zeta) d\xi, d\eta, d\zeta &= \int_{-1}^{+1} \int_{-1}^{+1} \int_{-1}^{+1} F(\xi, \eta, \zeta) d\xi, d\eta, d\zeta \\ &\simeq \sum_{i=1}^m \sum_{j=1}^n \sum_{k=1}^l F(\xi_i, \eta_j, \zeta_k) w_i w_j w_k \end{aligned} \quad (2.96)$$

where m, n, l denote the number of quadrature points (Gauss-points) in ξ, η, ζ directions, and w_i, w_j, w_k denote the corresponding weights. 2 Gauss points in each direction are used in this work.

2.9.4 Divergence Procedures

The modified Newton-Raphson method fails in some cases. Some simple but fairly effective procedures for handling divergence are discussed.

1. Under-relaxation : The iterative displacement is scaled

$${}^t\{\Delta u\}^{(i)} \leftarrow \alpha_u \{\Delta u\}^{(i)} \quad 0 < \alpha_u < 1 \quad (2.97)$$

where α_u is determined so that the numerical method does not diverge.

2. Line search : In this technique, the displacement vector is updated according to [38]

$${}^{t+\Delta t}\{u\}^{(i)} = {}^{t+\Delta t}\{u\}^{(i-1)} + \alpha_l {}^t\{\Delta u\}^{(i)} \quad (2.98)$$

and α_l is determined so that the unbalance (2.83) is minimum.

A full line search is computationally expensive. Therefore a cheaper technique is to evaluate unbalance at n different α_l values and choose

that α_l which corresponds to the minimum unbalance. This offers a good compromise between computational effort spent in line search and effort saved due to convergence in a reduced number of iterations.

3. Elastic response prediction : The elastic stiffness is used to predict the response and iterations are used to obtain the elasto-plastic response. This is beneficial when the structural response is highly stiffening and the loading is almost proportional in the increment.
4. Incremental displacement cutting : In case the procedures described above fail, incremental displacement cutting is performed.

2.10 Boundary Conditions for 3-D Forging of Rectangular Block

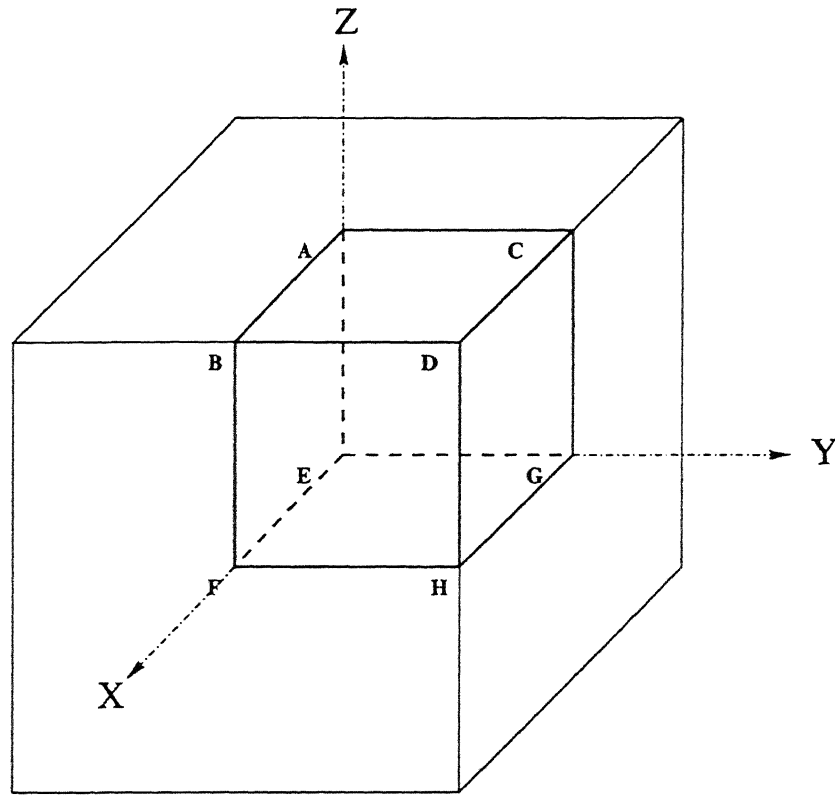


Figure 2.2: Boundary conditions for forging of a 3-D Rectangular Block

Figure (2.2) shows the domain of the problem. Due to symmetry, only $1/8$ th part of the workpiece is used for analysis. The boundary conditions for the domain of this problem are discussed below:

1 Workpiece-Die Interface (Plane ABCD)

In this study, it is assumed that the die surface is very rough. So complete sticking is assumed at the workpiece-die interface. Then the components of incremental displacement in x and y-direction are zero. Since this problem

is displacement controlled, the component of incremental displacement in z-direction is specified. Thus, boundary conditions on plane **ABCD** are :

Essential boundary conditions :

$$du_x = 0, du_y = 0, du_z = \text{specified} \quad (2.99)$$

2 Free Surfaces (Planes BDFH & CDGH)

These boundaries are traction free surfaces. Therefore, the boundary conditions on planes **BDFH & CDGH** are :

Natural boundary conditions :

$$dt_x = 0, dt_y = 0, dt_z = 0 \quad (2.100)$$

3 X-Y Plane of Symmetry (Plane EFGH)

Because of symmetry, normal component of incremental displacement and shear components of incremental traction vector are zero. Thus, the boundary conditions on plane **EFGH** are :

Natural boundary conditions :

$$dt_x = 0, dt_y = 0 \quad (2.101)$$

Essential boundary conditions :

$$du_z = 0 \quad (2.102)$$

4 X-Z Plane of Symmetry (Plane ABEF)

Because of symmetry, normal component of incremental displacement and shear components of incremental traction vector are zero. Thus, the boundary conditions on plane **ABEF** are :

Natural boundary conditions :

$$dt_x = 0, dt_z = 0 \quad (2.103)$$

Essential boundary conditins :

$$du_y = 0 \quad (2.104)$$

5 Y-Z Plane of Symmetry (Plane ACEG)

Because of symmetry, normal component of incremental displacement and shear components of incremental traction vector are zero. Thus, the boundary conditions on plane **ACEG** are :

Natural boundary conditions :

$$dt_y = 0, dt_z = 0 \quad (2.105)$$

Essential boundary conditins :

$$du_x = 0 \quad (2.106)$$

Chapter 3

Results And Discussion

The finite element model of 3-dimensional forging process developed in the previous chapter has been applied to a number of cases involving two materials and various sets of input variables to illustrate its applicability. The metals considered are Aluminium Al-1100 and Steel AISI 1019 (only in section 3.4.3) whose material properties are given as below. The properties for the aluminium are taken from [28] and that of the steel from [23].

Material properties:

Aluminium Al-1100

Young's modulus $E = 69 \text{ GPa}$

Poisson's ratio $\nu = 0.3$

Initial yield stress $(\sigma_y)_o = 62.74 \text{ MPa}$

Hardening coefficient $K = 90 \text{ MPa}$

Hardening exponent $n = 0.5377$

Steel AISI 1019

Young's modulus $E = 210 \text{ GPa}$

Poisson's ratio $\nu = 0.3$

Initial yield stress $(\sigma_y)_0 = 478.2 \text{ MPa}$

Hardening coefficient $K = 563.98 \text{ MPa}$

Hardening exponent $n = 0.14$

In this chapter, first a convergence study is performed to check the convergence of the finite element formulation with respect to displacement increment and mesh size. Then, the finite element code is validated by comparing the results with experimental results. In the last section, the parametric study is carried out to illustrate the effects of various process variables on the process parameters.

3.1 Convergence Study

The convergence study is performed for forging of a block of Al-1100 aluminium. Only 1/8 th of the block is considered for analysis (Fig. 3.1) due to symmetries in X, Y and Z planes. First, the convergence of forging load is checked. Then the convergence of stress distribution is studied. In each case, convergence is checked with respect to refinement in both the mesh size as well

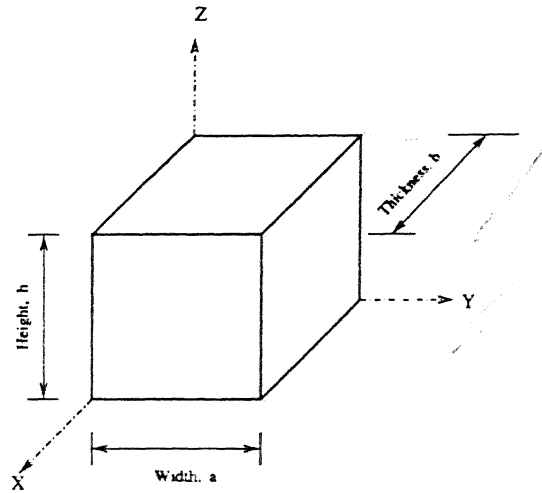


Figure 3.1: The domain used for analysis

as the increment size.

3.1.1 Convergence of Forging Load

The block dimensions chosen for this study are : $a = b = 9.525$ mm and $h = 4.7625$ mm. This size is the same as used in experimental studies of reference [28]. The reason for using this size is to facilitate the comparison with experimental results of reference [28].

Figure 3.2 shows the variation of forging load with % reduction for 4 different mesh sizes at the increment size of 0.025 mm. When the mesh is refined only in z-direction from $5 \times 5 \times 6$ elements to $5 \times 5 \times 12$ elements, it is observed that there is a large change in forging load (a decrease of 38.5 % at 20 % reduction). This happens because the condition of complete sticking is assumed at the die-workpiece interface which creates large displacement gradients in z direction. When the mesh is refined only in x and y directions

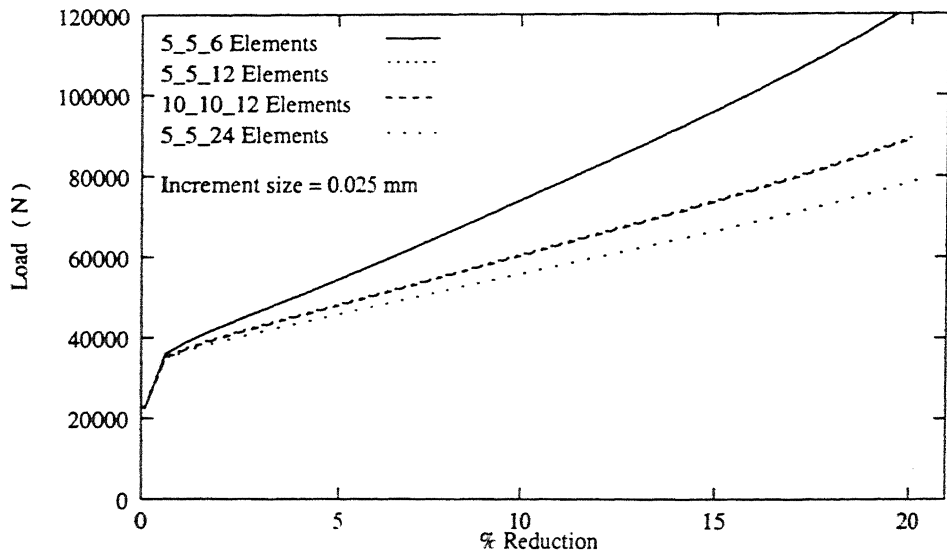


Figure 3.2: Convergence with mesh size

from $5 \times 5 \times 12$ to $10 \times 10 \times 12$ elements, it is found that there is no change in forging load. Thus, the displacement gradients doesn't seem to be large in x or y direction. A further refinement in z direction from $5 \times 5 \times 12$ elements to $5 \times 5 \times 24$ elements brings down the forging load by 14 % at 20 % reduction. This study shows that there is a trend towards convergence as the mesh size is refined. Analysis with the mesh of $5 \times 5 \times 24$ elements takes a lot of time. Therefore, it is decided to use the mesh size of $5 \times 5 \times 12$ elements in the further studies.

Figure 3.3 shows the variation of forging load with % reduction for 3 different increment sizes for the mesh of size of $5 \times 5 \times 12$ elements. It is observed that as the increment size is decreased from 0.05 mm to 0.025 mm, the forging load at 20 % reduction decreases by 9.28 %. A further reduction of the increment size to 0.0125 mm causes the reduction of forging load (at 20 % reduction) by 3.7 %. Thus, there is a trend towards convergence as the

increment size is decreased. It is decided to use the increment size of 0.025 mm for the rest of the study.

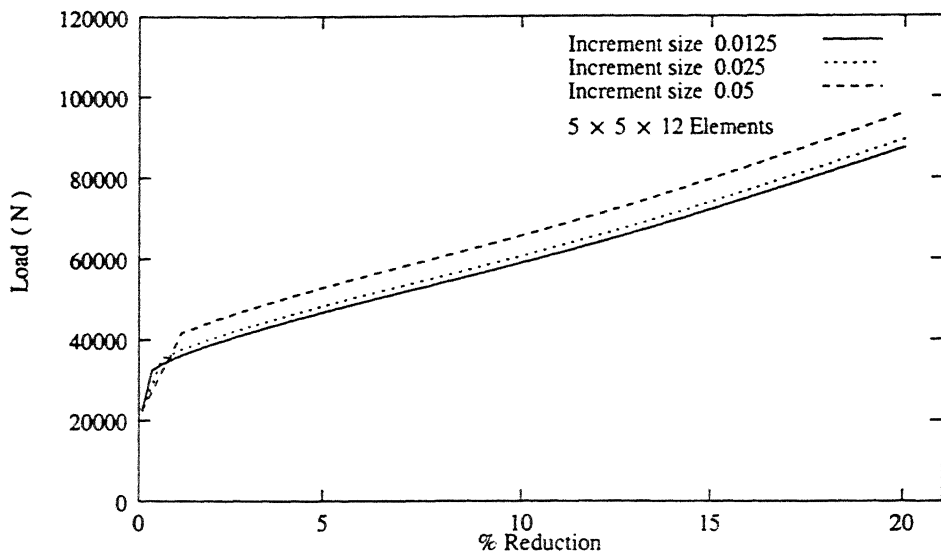


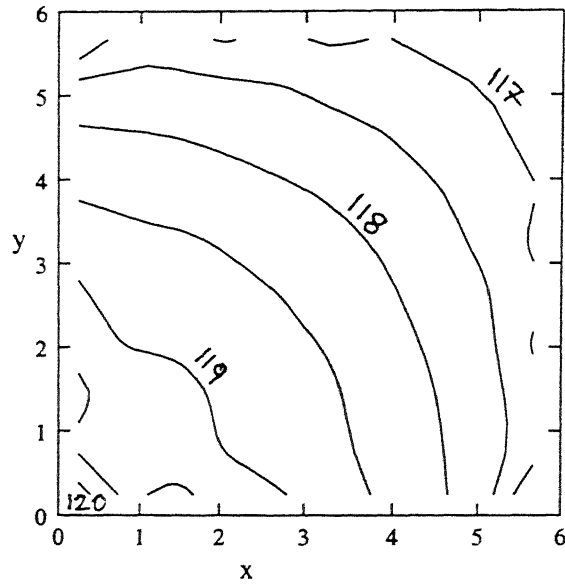
Figure 3.3: Convergence with increment size

3.1.2 Convergence of Stress Distribution

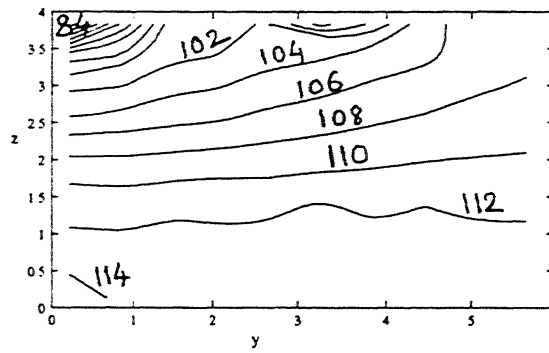
The block of $9.525\text{ mm} \times 9.525\text{ mm} \times 4.7625\text{ mm}$ was used for studying the convergence of forging load. The convergence was quite slow. Hence, it was decided to reduce the block size for studying the convergence of stress distribution. So, it was decided to use the size of $5\text{ mm} \times 5\text{ mm} \times 5\text{ mm}$.

Figures 3.4 to 3.11 show the equivalent stress distribution in x-y and y-z planes after 20 % reduction and after unloading for 3 different mesh sizes ($5 \times 5 \times 6$, $5 \times 5 \times 12$, $10 \times 10 \times 12$ elements) and 2 different increment sizes (0.025 mm, 0.0125 mm)¹. It is observed from Figs. 3.4-3.6 that the equivalent

¹The mesh size of $5 \times 5 \times 6$ means 6 elements in z direction and 5 elements each in x and y directions.



(a)



(b)

Figure 3.4: Equivalent stress distribution after 20 % reduction in (a) x_y (b) y_z planes for $5 \times 5 \times 6$ elements and increment size of 0.025 mm (in MPa)

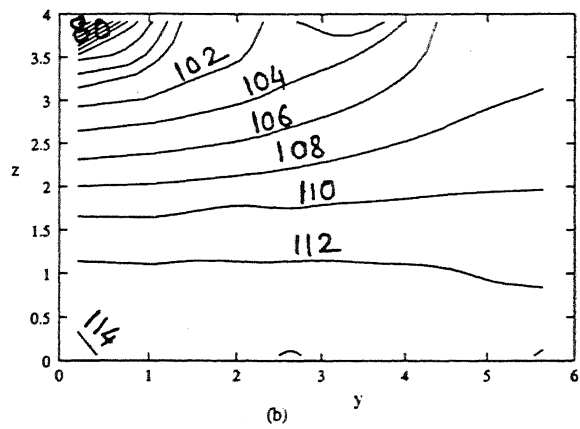
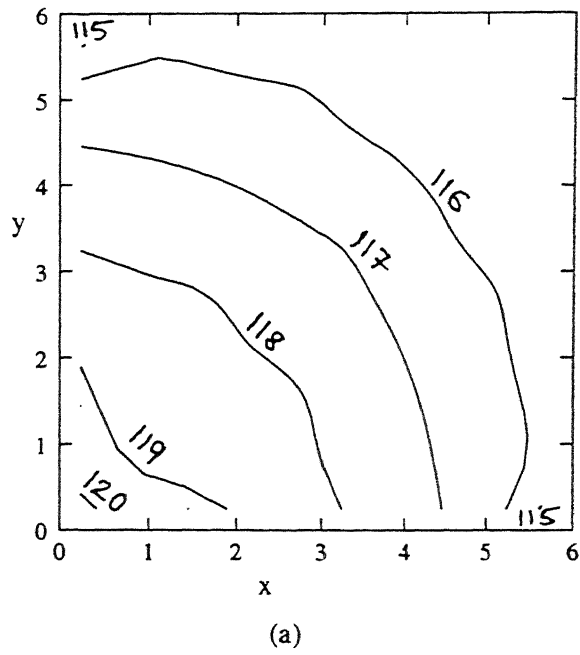
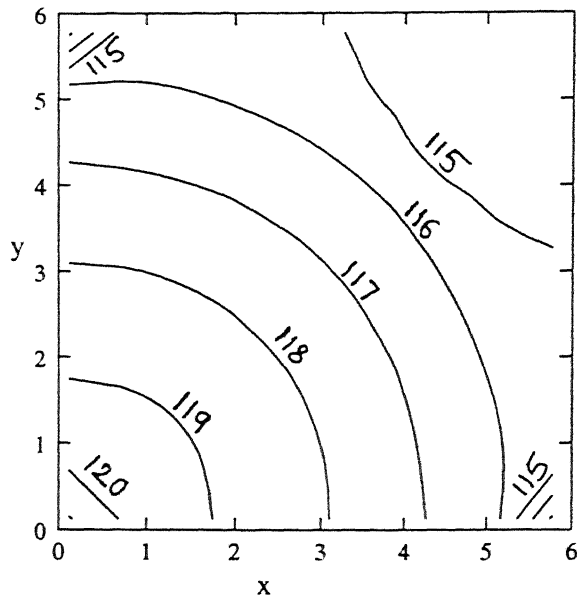
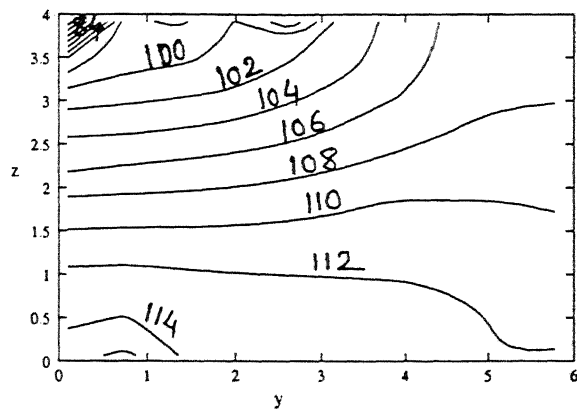


Figure 3.5: Equivalent stress distribution after 20 % reduction in (a) x-y (b) y-z planes for $5 \times 5 \times 12$ elements and increment size of 0.025 mm (in MPa)



(a)



(b)

Figure 3.6: Equivalent stress distribution after 20 % reduction in (a) x-y (b) y-z planes for $10 \times 10 \times 12$ elements and increment size of 0.025 mm (in MPa)

CENTRAL LIBRARY
I. T., KANPUR

No. A

127927

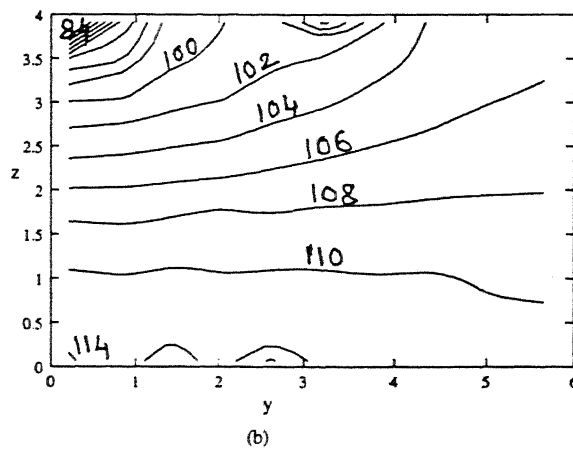
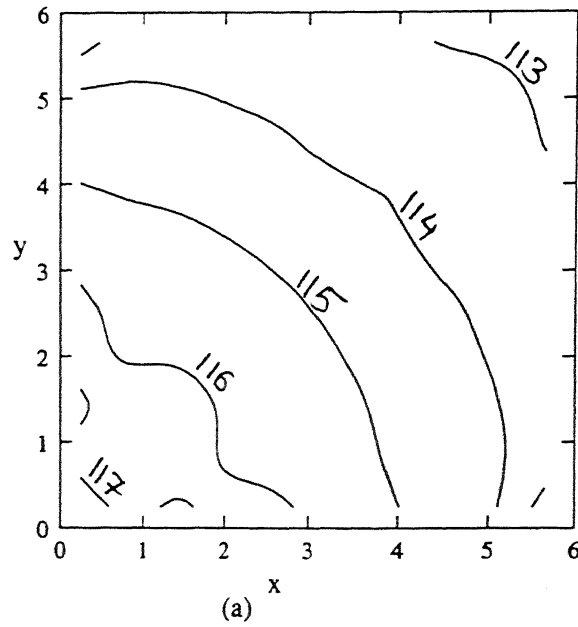


Figure 3.7: Equivalent stress distribution after 20 % reduction in (a) x-y (b) y-z planes for $5 \times 5 \times 12$ elements and increment size of 0.0125 mm (in MPa)

stress values (at 20 % reduction) converge as the mesh size is refined first from $5 \times 5 \times 6$ elements to $5 \times 5 \times 12$ elements and then to $10 \times 10 \times 12$ elements. The convergence is also observed when the increment size is decreased from 0.025 mm to 0.0125 mm (Figs. 3.5 and 3.7).

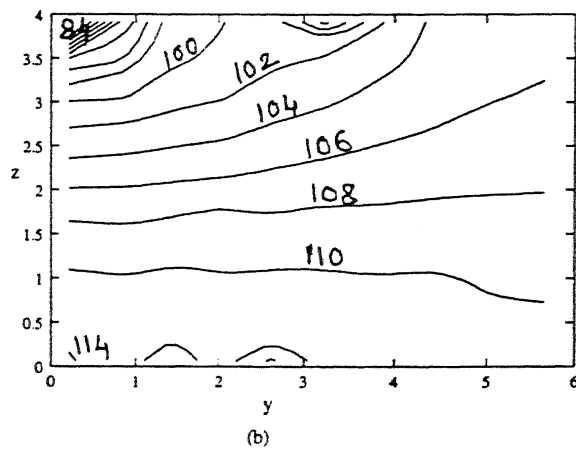
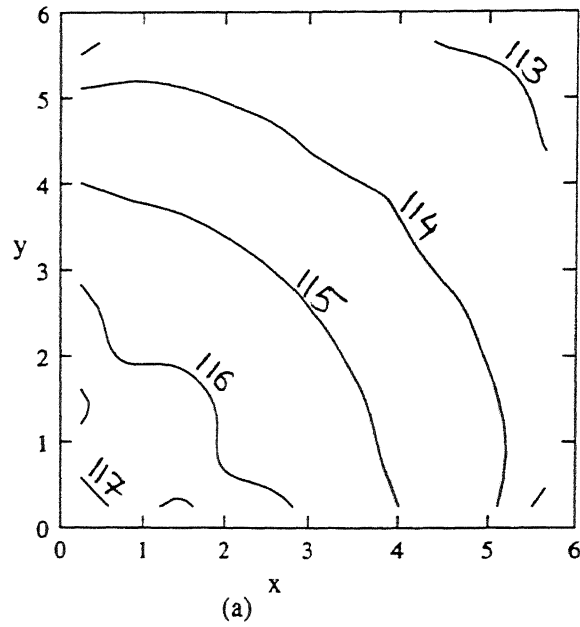
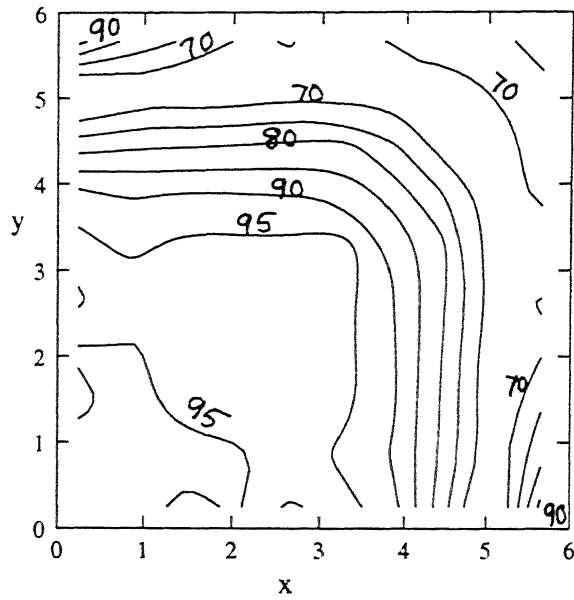


Figure 3.7: Equivalent stress distribution after 20 % reduction in (a) x-y (b) y-z planes for $5 \times 5 \times 12$ elements and increment size of 0.0125 mm (in MPa)

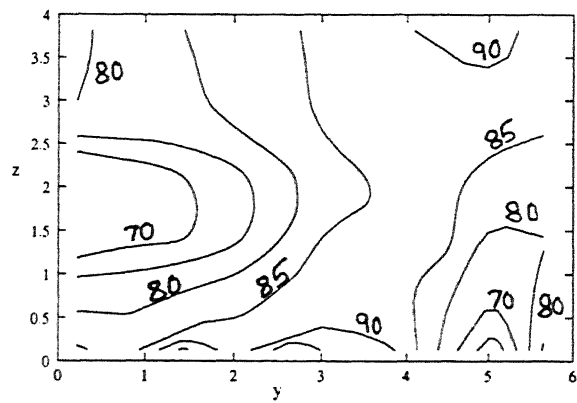
stress values (at 20 % reduction) converge as the mesh size is refined first from $5 \times 5 \times 6$ elements to $5 \times 5 \times 12$ elements and then to $10 \times 10 \times 12$ elements. The convergence is also observed when the increment size is decreased from 0.025 mm to 0.0125 mm (Figs. 3.5 and 3.7).

As far as the convergence of residual stresses is concerned, it is observed that the pattern of stress distribution in y-z plane changes when the mesh is refined in z direction from $5 \times 5 \times 6$ elements to $5 \times 5 \times 12$ elements (Figs. 3.8 and 3.9). The values also decrease drastically. As said in the last section, this happens due to large gradients in z direction arising due to the complete sticking condition at the interface. A refinement in x and y directions (see Figs. 3.9 and 3.10) does not cause much change in the pattern. But the maximum values do change by as much as 25 %. So the residual stress distribution, even though it shows a convergence trend, does not seem to have converged for the mesh size of $10 \times 10 \times 12$ elements. It was not possible to make further refinement. Even the mesh of $10 \times 10 \times 12$ elements takes a lot of time for determination of residual stresses at 20 % reduction. So it was decided to use the mesh of $5 \times 5 \times 12$ elements with the understanding that the values would be off at least by 25 %. When the increment size is decreased from 0.025 mm to 0.0125 mm, however, the residual stresses do converge (Figs. 3.9 and 3.11). So it was decided to use the increment size of 0.025 mm in the rest of the study.

It is observed that, in all the cases, the equivalent stress distribution (both after 20 % reduction and after unloading) in x-z plane (not shown here) is exactly identical to that in y-z plane. This is because the width of the block (dimension in y direction) is equal to its thickness (dimension in x direction).

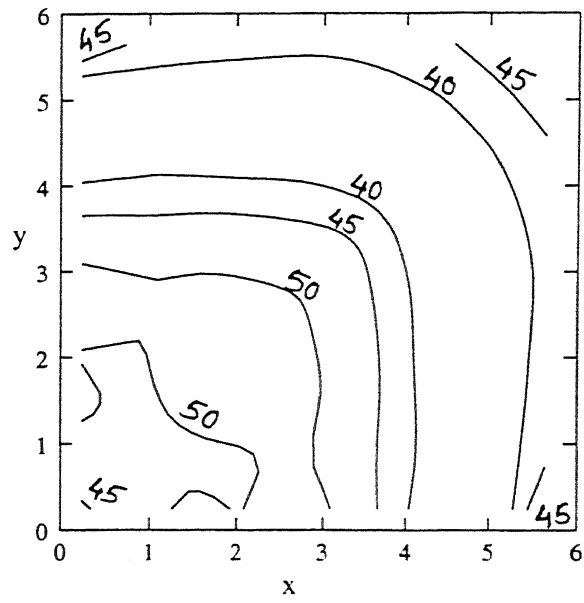


(a)

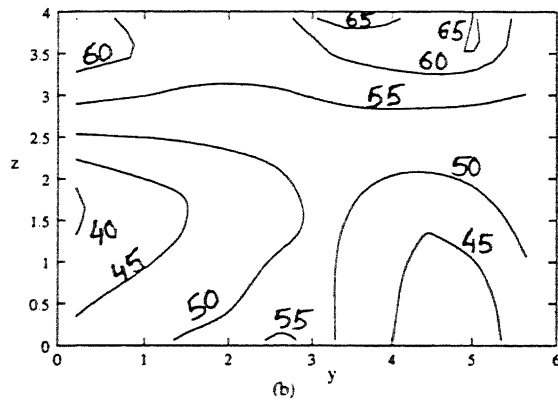


(b)

Figure 3.8: Residual equivalent stress distribution after unloading in (a) x - y (b) y - z planes for $5 \times 5 \times 6$ elements and increment size of 0.025 mm (in MPa)

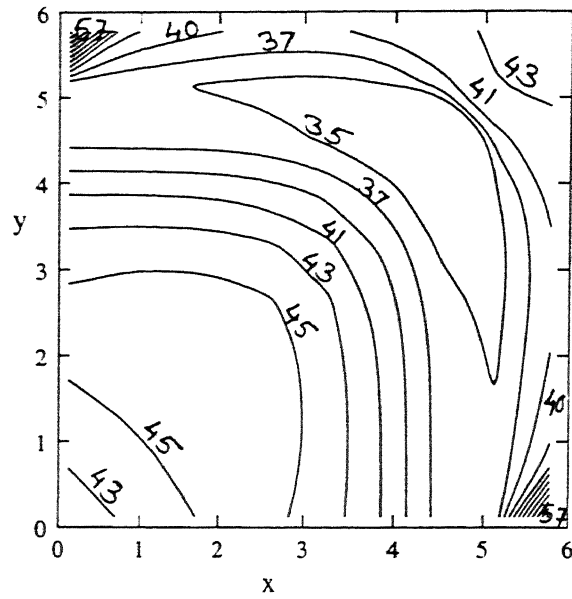


(a)

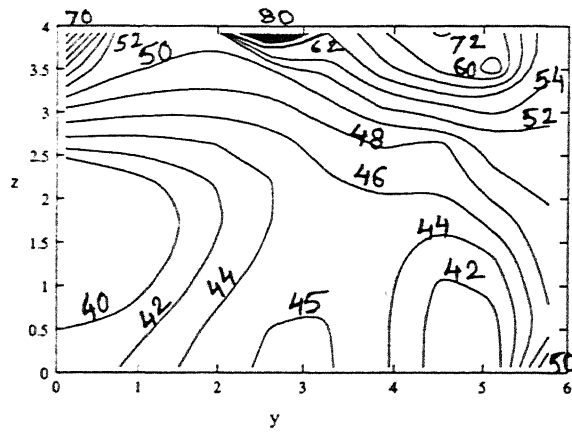


(b)

Figure 3.9: Residual equivalent stress distribution after unloading in (a) x - y (b) y - z planes for $5 \times 5 \times 12$ elements and increment size of 0.025 mm (in MPa)

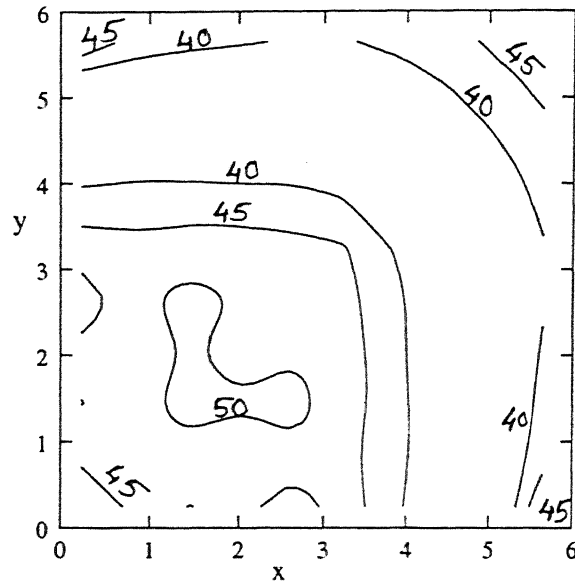


(a)

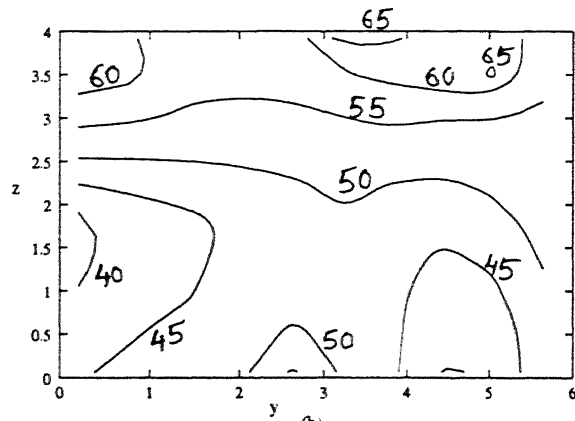


(b)

Figure 3.10: Residual equivalent stress distribution after unloading in(a) x-y (b) y-z planes for $10 \times 10 \times 12$ elements and increment size of 0.025 mm (in Mpa)



(a)



(b)

Figure 3.11: Residual equivalent stress distribution after unloading in (a) x-y (b) y-z planes for $5 \times 5 \times 12$ elements and increment size of 0.0125 mm (in MPa)

3.2 Validation

The FEM code is validated by comparing the results on forging load with experimental results of [28]. The block material is Al-1100 aluminium and has

the dimensions of $19.05\text{ mm} \times 19.05\text{ mm} \times 9.525\text{ mm}$. Lubricated condition at the interface is maintained in the experimental studies of [28]. The FEM analysis is done using only $1/8$ of the block, $5 \times 5 \times 12$ elements and increment size of 0.025 mm . Complete sticking at the interface is assumed in the FEM analysis.

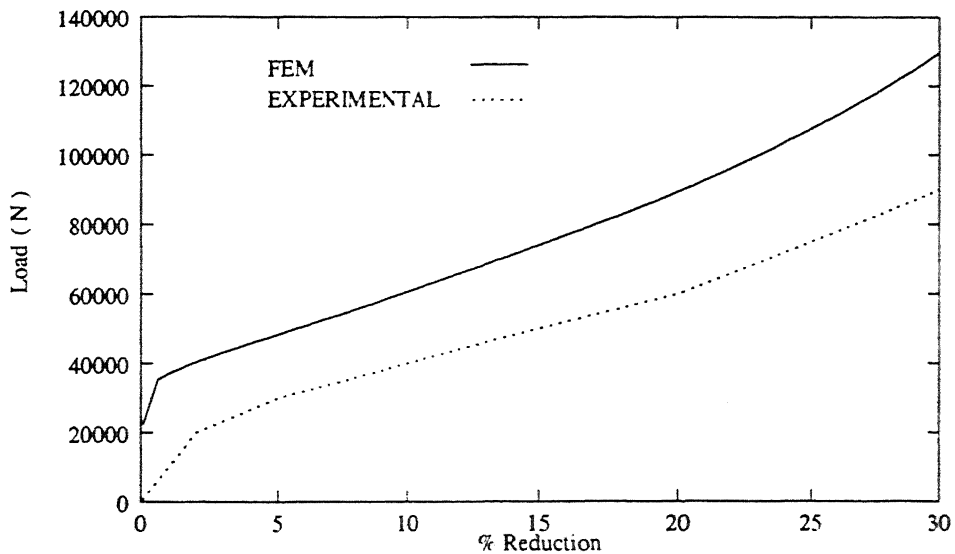


Figure 3.12: Comparison of theoretical and experimental [28] load-displacement curves.

Fig. (3.12) shows the comparison of FEM and experimental load-displacement curves. The discrepancy between the theoretical and experimental predictions can be explained as follows. In experimental studies, as the die-workpiece interface is lubricated, slip is observed over a part of the interface, whereas in this FEM modelling, full sticking is assumed over the whole interface. As a result, the elements on the free surface near the edge undergo a very large deformation. But in the experimental studies, the deformation is not so large due to the slip at the interface. Even though the FEM model neglects the interfacial slip, the energy needed to create the above mentioned

large deformation of the free surface elements seems to be more than what is dissipated due the interfacial slip. This is the reason why the theoretically predicted values of the forging load are higher than the experimental values.

3.3 Analysis of Forging Parameters for Typical Case

In this section, various forging parameters like the equivalent stress distribution, residual stress distribution, contact pressure distribution, bulge profile etc are discussed for a typical block of $5\text{ mm} \times 5\text{ mm} \times 5\text{ mm}$ size and made up of Al-1100 aluminium. The mesh of $5 \times 5 \times 12$ elements and the increment size of 0.025 mm used. The analysis is carried out up to 20% reduction in height.

Contact pressure:

Figure (3.13) shows the contact pressure distribution at the die-workpiece interface. The contact pressure is minimum at the center of the interface and increases in both the width-wise and thickness-wise directions. It attains a maximum value at the free corner. The high value at the free corner is the result of complete sticking at the interface.

Equivalent stress after loading:

Figure 3.5 shows the contours of equivalent stress in x-y and y-z planes. It shows that the entire domain has yielded as every where $\sigma_{eq} > 62.74\text{ Mpa}$, the initial yield stress. In x-y plane, the equivalent stress is maximum at the origin of x and y axes (i.e. at the center of block) and decreases in the

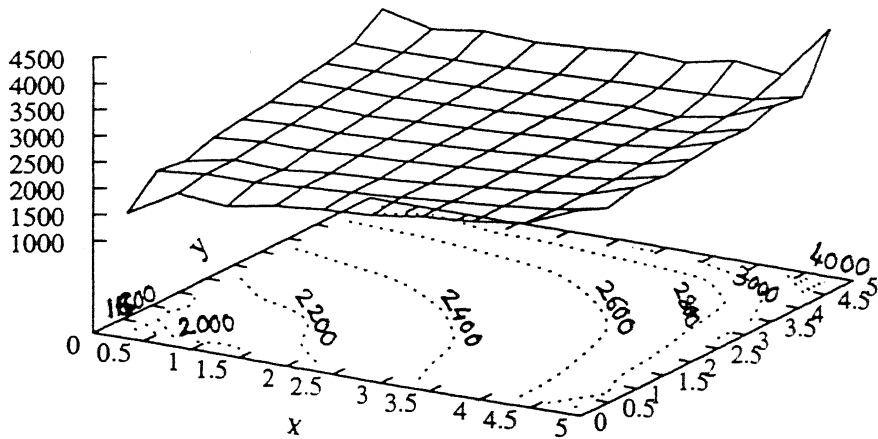


Figure 3.13: distribution of contact pressure (in MPa)

diagonal direction towards the free corner. In y-z plane also, the maximum value of equivalent stress occurs at the center. But, here stress decreases in the upward direction. The minimum value, however, does not occur along the entire interface but only at the center of the interface.

It is observed that the contours of equivalent stress in x-z plane (not shown here) are identical to that in y-z plane. This is because the width of the block (dimension along y direction) is equal to its thickness (dimension along x direction)

Bulge profile after loading:

The bulge profile after loading is shown in Fig (3.14). The bulge is more along x and y axes than at the free corner.

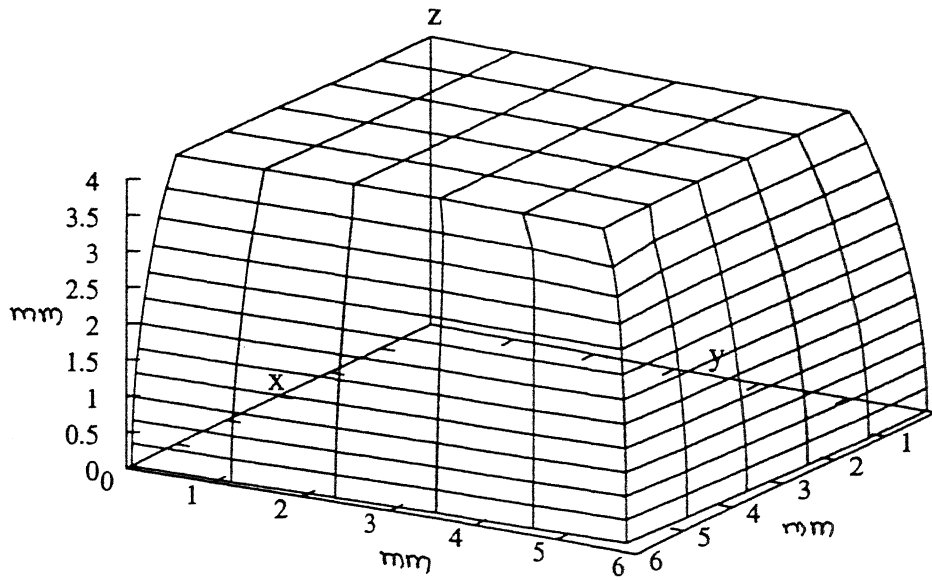


Figure 3.14: bulge profile after loading

Residual stresses :

Figure 3.9 shows the contours of residual equivalent stress (after unloading) in x-y and y-z planes. The pattern of these distributions are different than those of equivalent stress after loading. Further, the values are less. In x-y plane, all the values are less than the initial yield stress (62.74 Mpa). The maximum value now is not at the origin of x and y axes but somewhere in the middle of the plane. In y-z plane, along the interface, there are pockets of $\sigma_{eq} > 62.74 \text{ Mpa}$. The maximum value of residual equivalent stress occurs in this region.

Due to geometric symmetry ($a = b$), the residual equivalent stress distribution in x-z plane is exactly identical to that in y-z plane. That is why it is not shown here.

Bulge profile after unloading:

The bulge profile after unloading is shown in Fig. (3.15). During unloading, only the elastic deformation is recovered, therefore there is only a small change in shape and size from the bulge profile of Fig. 3.14 .

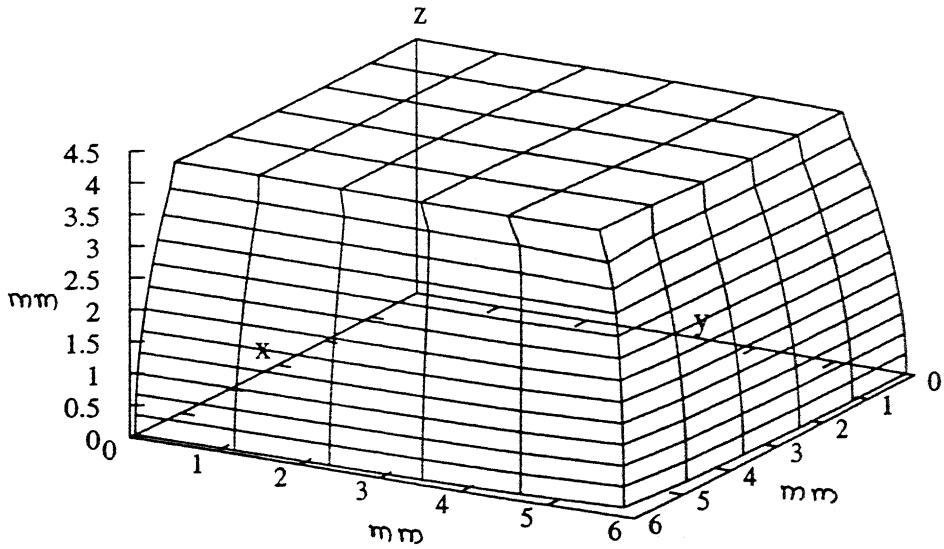


Figure 3.15: bulge profile after unloading

3.4 Parametric Study

In this section, a study is made of the effects of process variables viz. the percent reduction in height, the geometric ratios h/a and b/a and the material properties on the equivalent stress distribution after loading and the residual stress distribution.

The mesh of $5 \times 5 \times 12$ elements and the incremental displacement of 0.025 mm is used in this study.

3.4.1 Effects of Geometric Ratios (h/a and b/a)

The effects of geometric ratios h/a (height to width ratio) and b/a (thickness to width ratio) are studied by carrying out the analysis for the following 3 cases. Case 1 : $h/a = 1$, $b/a = 1$, Case 2 : $h/a = 0.6$, $b/a = 1$ and Case 3 : $h/a = 1$, $b/a = 0.6$. The value of ~~a~~ ^{t} used is 5 mm. The analysis is carried out up to 20 % reduction and the material used is Al-1100 aluminium. For the case 1, the equivalent stress distribution after loading and the residual equivalent stress distribution both in x-y and y-z planes are already shown in Figures 3.5 and 3.9. The distributions in x-z plane are identical to those in y-z plane and hence are not shown.

When the height of the block is reduced (case 2), then the stress distribution in x-y plane doesn't change. This is as expected. However, when

the thickness b (dimension along y axes) of the block is reduced compared to its width a (dimension along x axes), i.e. in case 3, it was expected that the equivalent stress distribution in x - y plane would change. But it doesn't change. Since the stress distribution in x - y plane for all the three cases is identical, it is shown here only for the case 1 (Fig. 3.5).

The equivalent stress distribution in y - z plane certainly changes for the case 2, i.e when the height of the block is reduced (see Figures 3.5 and 3.16). The maximum and minimum values change by a small amount. Because of the geometric symmetry ($b = a$), the distribution in x - z plane is exactly identical and that is why it is not shown. It was expected that when b is reduced compared to a (case 3), the stress distribution in y - z plane would change. But, comparison of Figure 3.5 and 3.17 shows that, it doesn't happen. It was also expected that, now since the geometric symmetry does not exist ($b \neq a$), the distribution in x - z plane would be different than that in y - z plane. But, this also doesn't happen (see Fig. 3.17).

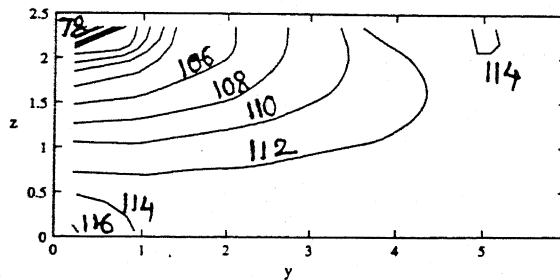


Figure 3.16: Equivalent stress distribution after 20 % reduction in y - z plane for $h/a=0.6$ (in MPa)

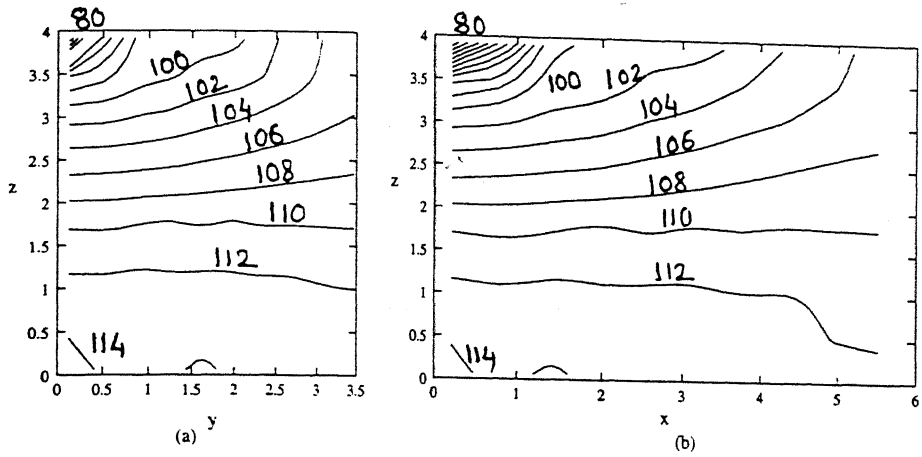


Figure 3.17: Equivalent stress distribution after 20 % reduction in (a) y-z (b) x-z planes for $b/a=0.6$ (in MPa)

The pattern of residual equivalent stress distribution in x-y plane doesn't change much for the case 2, i.e. when the height of the block is reduced (see Figures 3.9 and 3.18). However, the value of maximum stress becomes almost double the value for case 1. Further its location shifts to the end of y axes. For the case 3, i.e. when b is decreased compared to a, the residual stress distribution becomes unsymmetric with respect to x and y directions (see Fig. 3.20). Also, the value of maximum residual stress increases. Further, its location shifts to the origin of x and y axes. Thus, it can be concluded that the values of residual stresses increase when any one dimension is decreased, the increase being more when the height is decreased.

The residual equivalent stress distribution in y-z plane changes when the height of the block is reduced, i.e. for the case 2 (see Figures 3.9 and 3.19). Further, the value of maximum stress increases substantially even though its location doesn't change. The distribution in x-z plane (not shown) is identical to that in y-z plane. For the case 3 (i.e. when b is reduced compared to

a), it was expected that the residual stress distribution in y-z plane would change. But, comparison of Figures 3.9 and 3.21 shows that it doesn't happen. However, the distribution in x-z plane is different than that in y-z plane. The value of maximum residual stress is also slightly higher.

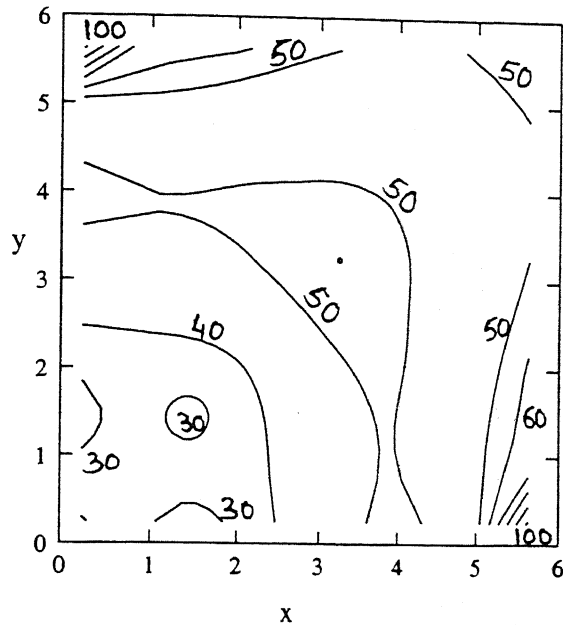


Figure 3.18: Residual equivalent stress distribution after unloading in x-y plane for $h/a=0.6$ (in MPa)

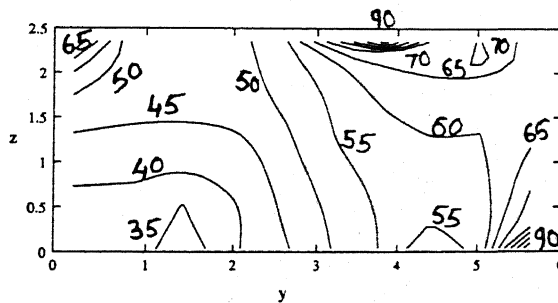


Figure 3.19: Residual equivalent stress distribution after unloading in y-z plane for $h/a=0.6$ (in MPa)

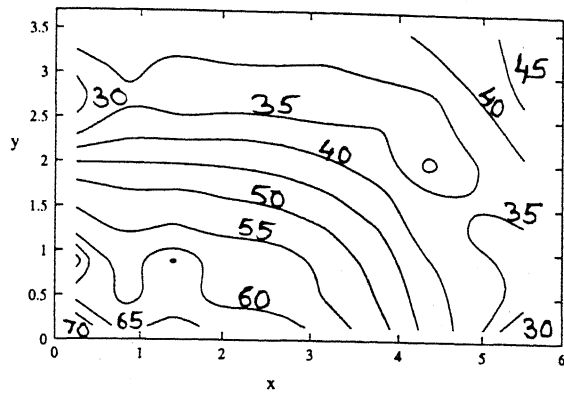


Figure 3.20: Residual equivalent stress distribution after unloading in x-y plane for $b/a = 0.6$ (in MPa)

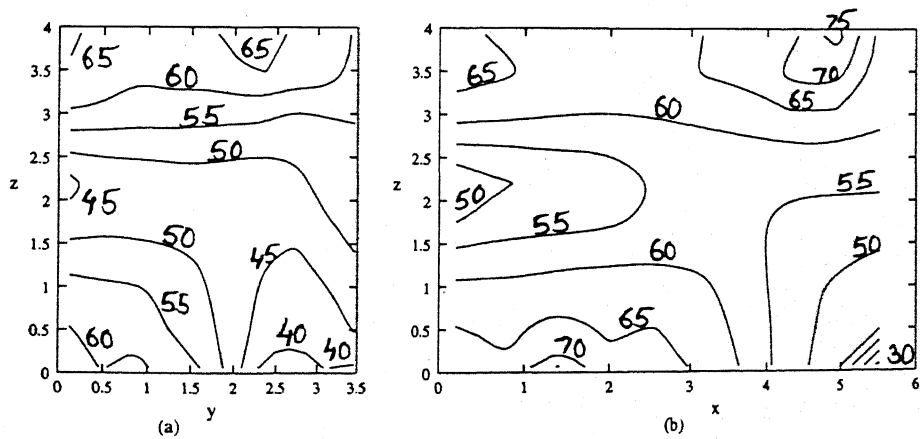


Figure 3.21: Residual equivalent stress distribution after unloading in (a) y-z (b) x-z planes for $b/a = 0.6$ (in MPa)

3.4.2 Effect of Percentage Reduction in Height

The effect of percentage reduction ($\% r$) is studied by analysing the problem for 2 different values of r : 20 % and 10 %. The material used is Al-1100 aluminium and the geometric ratios are $h/a = 1$ and $b/a = 1$ with $a = 5$ mm. For 20 % reduction, the equivalent stress distribution after loading and residual equivalent stress distribution are already presented in Figure 3.5 and 3.9.

When the percentage reduction is reduced, the pattern of equivalent stress distribution doesn't change. However, as expected, the value of maximum equivalent stress decreases with a reduction in $\% r$. At 20 % reduction, the value of maximum equivalent stress is 120 Mpa (Fig. 3.5) which reduces to 102 Mpa at 10 % reduction.

As far as the pattern of residual equivalent stress distribution is concerned, it also doesn't change much when the reduction is reduced to 10 % (see Figures 3.22 - 3.23). However, as expected, the value of maximum residual equivalent stress decreases with a reduction in $\% r$. The maximum value decreases from 65 Mpa (Fig. 3.9) at 20 % reduction to 55 Mpa at 10 % reduction. Thus, at 10 % reduction, all the residual equivalent stress values are less than the yield stress (62.74 Mpa).

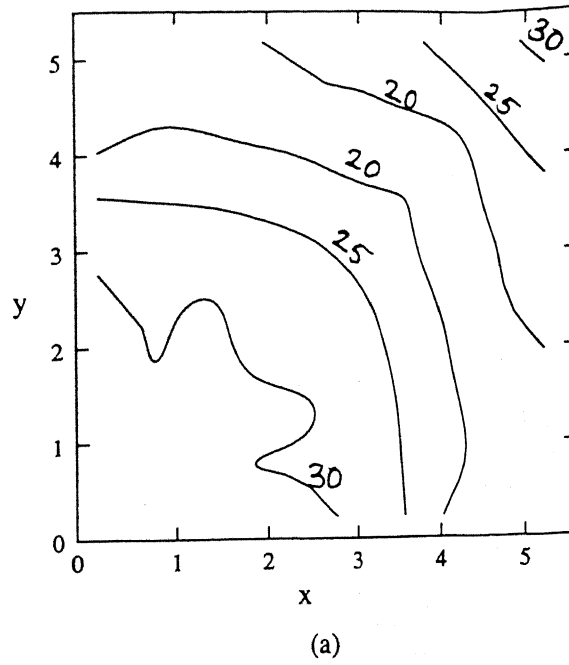


Figure 3.22: Residual equivalent stress distribution after unloading in x-y plane for 10 %reduction (in MPa)

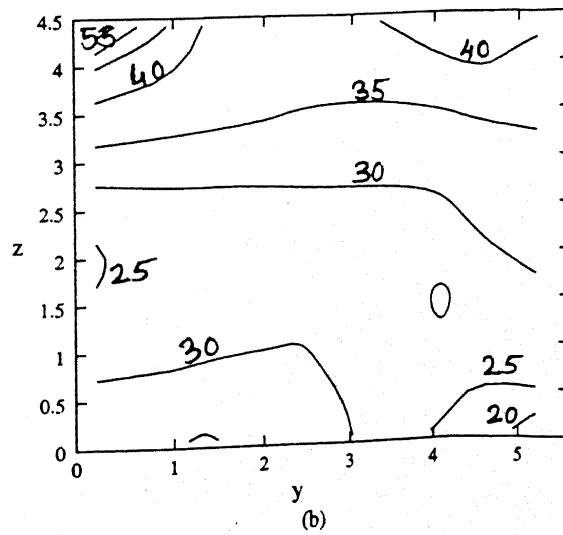
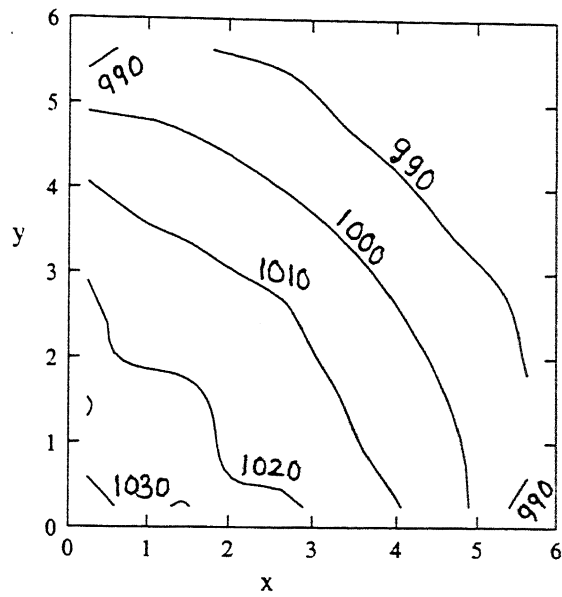


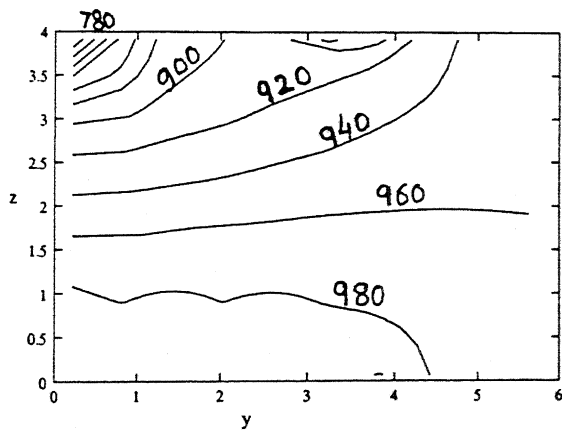
Figure 3.23: Residual equivalent stress distribution after unloading in y-z plane for 10 %reduction (in MPa)

3.4.3 Effect of Material Properties

The effect of material properties is analysed by considering 2 different materials : Al-1100 aluminium and AISI-1019 steel. The analysis is done up to 20 % reduction and for the geometric ratios of $h/a = 1$ and $b/a = 1$ (with $a = 5$ mm). The equivalent stress distribution after unloading and the residual equivalent stress distribution for the case of aluminium are already shown in Figures 3.5 and 3.9 . For the steel, these distributions are shown in Figures 3.24 and 3.25. Comparison of these Figures shows that the pattern of both these distributions for the steel is the same as that for the aluminium. However, the maximum values are more for the steel. The maximum equivalent stress for aluminium is 120 Mpa (Fig. 3.5) whereas for the steel, it is 1030 Mpa (Fig. 3.24). Similarly, the maximum residual equivalent stress for aluminum is 65 Mpa (Fig. 3.9), but for steel, it is 660 Mpa (Fig. 3.25). Just as in the case of aluminium, only in a small part of the y-z plane, the residual equivalent stress exceeds the yield stress (which is 478.2 Mpa for the steel).

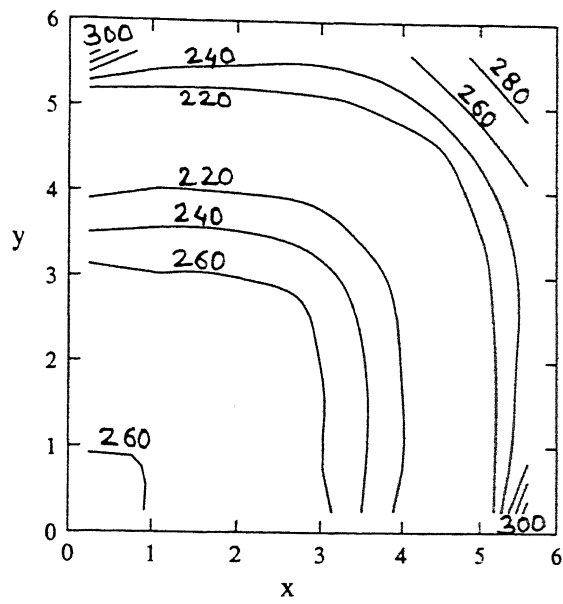


(a)

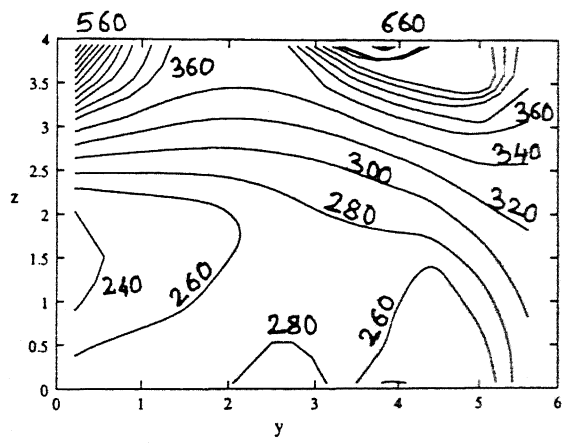


(b)

Figure 3.24: Equivalent stress distribution after 20 % reduction for steel in (a) x-y (b) y-z planes (in MPa)



(a)



(b)

Figure 3.25: Residual equivalent stress distribution after unloading for steel in (a) x-y (b) y-z planes (in MPa)

Chapter 4

Conclusions and Scope for Future work

The objective of this work is to develop a 3-D large deformation elasto-plastic finite element code for determination of residual stresses in cold forging process. The updated Lagrangian formulation which is convenient for handling material and geometric nonlinearities is used. New incremental objective stress measure and logarithmic strain measure are used which can allow the use of large incremental displacement. Forging process is a displacement controlled problem. Therefore, to accelerate the convergence of the iterative scheme, arc length method is used in conjunction with modified Newton Raphson iterative technique. The detailed parametric study of residual stresses has been presented to show the effects of three process variables namely the percentage reduction in height, the geometric ratios and the material properties. For a typical case, the normal stress stress distribution at the die-workpiece interface and the deformation patterns after loading and unloading have been presented. The following conclusions can be drawn :

- After loading, the equivalent stress is maximum at the center of the block, but after unloading the maximum residual equivalent stress occurs at the die-workpiece interface.
- From parametric study, it can be concluded that the values of residual stresses increase when any one dimension is decreased, the increase being more when the height is decreased.
- The material properties have no effect on the pattern of either the equivalent stress distribution after loading or the residual stress distribution.
- The % reduction also has no effect on the pattern of the equivalent stress distribution after loading as well as the residual stress distribution. The values of residual stress increases with % reduction.

The following work may be taken up as extensions of the present study :

- Proper modelling of interfacial friction and slip.
- Dependence of material behaviour on strain rate (viscoplasticity) and temperature.
- Analysis and prediction of defects in forging process during loading and due to residual stresses.
- A preprocessor and postprocessor are a must for generation of input data and interpretation of results in a complicated 3-D analysis.

References

- [1] **J. N. Majerus**, "Qualitative data for precision, closed die forging via line averaged residual plastic-strains", *Int. J. Mach. Tools Manufact.*, vol. 37(5), pp. 657-667, 1997.
- [2] **L. Prandtl**, "Anwendungsbeispiele zu henckyschen Staz uber das plastische gleichgewicht", *Zeitschrift Angewandte Mathematik und Mechanik*, vol. 3, pp. 401-406, 1923.
- [3] **R. Hill, E. H. Lee and S. J. Tupper**, "A method of numerical analysis of plastic flow in plane strain and its application to the compression of a ductile material between rough plates", *Trans. of ASME, J. Appl. Mech.*, vol. 73, pp. 46-52, 1923.
- [4] **A. P. Green**, "A thereotical investigation of the compression of a ductile material between smooth flat dies", *Philosophical Magazine Series 7*, vol. 42, pp. 900, 1951.
- [5] **A. Shabaik**, "Prediction of the geometric changes of the free boundary during upsetting by the slip-line theory", *ASME paper no. 70-WA/prd-17*.
- [6] **O. Hoffman and G. Sachs**, "Introduction to the Theory of Plasticity for Engineers", *McGraw-Hill Book Company, New York*, 1953.
- [7] **T. Altan**, "Computer simulation to predict load, stress and metal flow in an axisymmetric closed-die forging", in *Metal Forming*, ed. Hoffmann, A.L., pp. 325-347, Plenum Press, 1971.

- [8] **W. Prager and P. G. Hodge**, " Theory of Perfectly Plastic Solids ",
John Willy, New York, 1951.
- [9] **P. C. Drucker**, " Coloumb friction, plasticity and limit loads", *Trans. of ASME, J. Appl Mech.*, vol. 21, pp. 71-74, 1954.
- [10] **H. Kudo**, " Some analytical and experimental studies of axi-symmetric cold forging and extrusion-I and II", *Int. J. Mech . Sci.*, vol. 2, pp. 102-127, 1960.
- [11] **H. Kudo**, " An upper bound approach to plane-strain forging and extrusion-I and II", *Int. J. Mech. Sci.*, vol. 2, pp. 57-83, 1960.
- [12] **B. Avitzur**, " A Metal Forming: Process and Analysis", *McGraw Hill Book Company, New York, 1968.*
- [13] **S. Kobayashi**, " Upper bound solution of axisymmetric forming problems, parts I and II", *Trans ASME, ser. B*, vol. 86, no. 4, pp. 326-332, 1964.
- [14] **A. G. MacDonald, S. Kobayashi and E. G. Thomsen**, " Some problems of press forging lead and aluminum", *Trans . ASME, ser. B*, vol. 82, pp. 246-252, 1964.
- [15] **D. Y. Yang and J. H. Kim** , "An analysis of three-dimensional upset forging of regular polygonal blocks by using the upper-bound method", *Trans. of ASME J. Engr. for Ind.*, vol. 109, pp. 155-160, 1987.

- [16] **J. H. Kim., D. Y. Yang and M. U. Kim,** "Analysis of three-dimensional upset forging of arbitrarily-shaped prismatic blocks ", *Int. J. Mach. Tools Manufact.*, vol. 27(3), pp. 311-323, 1987.
- [17] **Manuel J. M., Barata Marques and Paulo A. F. Martins,** "The use of dual-stream functions in the analysis of three-dimensional metal forming processes ", *Int. J. Mech. Sci.*, vol. 33, pp. 313-323, 1991.
- [18] **C. H. Lee and S. Kobayashi,** " Analysis of axisymmetric upsetting and plane-strain side-pressing of solid cylinders by the finite element method", *Trans. ASME, J. Engr. for Ind.*, vol. 93, pp. 445-454, 1971.
- [19] **S. N. Shah, Lee, C. H. Lee and S. Kobayashi,** " Compression of tall, circular solid cylinders between parallel flat dies", *Proc. Int. Conf. Prod. Engr., Tokyo*, pp. 865, 1973.
- [20] **C. C. Chen and S. Kobayashi,** " Rigid -plastic finite element analysis of ring compression: applications of numerical method of forming processes", *ASME, AMD*, vol. 28, pp. 163, 1978.
- [21] **S. I. Oh and S. Kobayashi,** " Workability of aluminum alloy 7075-T6 in upsetting and rolling", *Trans. ASME, J. Engr. for Ind.*, vol. 98, pp. 800-806, 1976.
- [22] **G. Maccarini, C. Pellegrini and A. Bugini,** "The influence of die geometry on cold extrusion forging operations: FEM and experimental results", *J. Mater. process. Technol.*, vol. 27, pp. 227-238, 1991.

- [23] P. Hartely, C. E. Sturgess and G. W. Rowe , " Influence of friction on the prediction of forces, pressure distributions and properties in upset forging", *Int. J. Mech. Sci.*, vol. 22, pp. 743-753, 1980.
- [24] P. Hartely, C. E. Sturgess and G. W. Rowe , " Friction in finite element analysis of metal forming process", *Int. J. Mech. Sci.*, vol. 21, pp. 301-311, 1975.
- [25] I. Pillinger, P. Hartley, C. E. N. Sturgess and G. W. Rowe, "An elastic-plastic three-dimensional finite element analysis of the upsetting of rectangular blocks and experimental comparison ", *Int. J. Mach. Tool Des. Res.*, vol. 25(3), pp. 229-243, 1985.
- [26] K. J. Bathe, E. Ramm and E. L. Wilson, " Finite element formulations for large deformation dynamics analysis", *Int. J. Num. Meth. En-gng.*, vol. 9, pp. 353-386, 1975.
- [27] W. T. Carter, Jr and D. Lee, " Further analysis of axisymmetric up-setting", *Trans. ASME, J. Engr. for Ind.*, vol. 108, pp. 198, 1986.
- [28] J. J. Park and Kobayashi, "Three-dimensional finite element analysis of block compression ", *Int. J. Mech. Sci.*, vol. 26(3), pp. 165-176, 1984.
- [29] Han-Ho Choi, Jin-Hee Lee, Sang-Kyu Bijun and Beom-Soo Kang. "Development of a three dimensional finite-element program for metal forming and its applications to precision coining ", vol. 72, pp. 396-402, 1997.

- [30] **Jan Terziyski, Tatsuhiko Aizawa and Junji Kihara**, "Three dimensional forging simulation with finite element control", *J. Mater. process. Technol.*, vol. 45, pp. 75-80, 1994.
- [31] **G. Surdon and J. L. Chenot**, "Finite element calculation of three-dimensional hot forging", *Int. J. Num. Meth. Engng.*, vol. 24, pp. 2107-2117, 1987.
- [32] **Mingwang Fu and Zijian Luo**, "The prediction of macro-defects during the isothermal forging process by the rigid-viscoplastic finite-element method ", *J. Mater. process. Technol.*, vol. 32, pp. 599-608, 1992.
- [33] **J. H. Liou and D. Y. Jang**, "Forging parameter optimization considering stress distributions in products through FEM analysis and robust design methodology ", *Int. J. Mach. Tools Manufact.*, vol. 37(6), pp. 775-782, 1997.
- [34] **V. Satyanarayan**, "Dynamic large deformation elasto-plastic analysis of continua ", *M.Tech Thesis, Dept. of Mech. Engg., I.I.T. Kanpur*, 1997.
- [35] **C. Truesdell**, "The Elements of Continuum Mechanics", *Springer-Verlag, New York*, 1966.
- [36] **J. K. Dienes**, "On the analysis of rotation and stress rate in deforming bodies ", *Acta Mechanica*, vol. 32, pp. 217-232, 1979.
- [37] **D. P. Flanagan and L. M. Taylor**, "An accurate numerical algorithm for stress integration with finite rotations ", *Comp. Meth. Appl. Mech. Engng.*, vol. 62, pp. 305-320, 1987.

- [38] **M. A. Crisfield**, "Non-linear Finite Element Analysis of Solids and Structures", *Volume 1, Essentials. Chichester, John Wiley and sons, 1994.*
- [39] **D. R. Metzger and R. N. Dubey**, "Objective tensor rates and frame indifferent constitutive models", *Mechanics Research Communications, vol. 13(2), pp. 91-96, 1986.*
- [40] **E. H. Lee**, "Some comments on elastic-plastic analysis ", *Int. J. Solids Structures, vol. 17, pp. 859-872, 1981.*
- [41] **D. R. J. Owen and E. Hinton**, " Finite Elements in Plasticity: Theory and Practice", *Pineridge Press, Swansea, UK, 1980.*
- [42] **K. J. Bathe**, "Finite Element Procedures ", *Prentice-Hall of India, New Delhi, 1998.*
- [43] **O. C. Zienkiewicz**, "The Finite Element Method ", *Tata McGraw-Hill, 1990.*
- [44] **B. Irons and S. Ahmad** , "Techniques of Finite Elements ", *Ellis-Horwood, Chichester, 1980.*
- [45] **J. Chakrabarty**, " Theory of Plasticity", *McGraw-hill Book Company, Singapore, 1987.*
- [46] **W. E. Haisler and J. A. Stricklin**, "Displacement incrementation in non-linear structural analysis by the self-correcting method ", *Int. J. Num. Meth. Engng., vol. 11, pp. 3-10, 1977.*

- [47] **J. L. Batoz** and **G. Dhatt**, "Incremental displacement algorithms for nonlinear problems ", *Int. J. Num. Meth. Engng.*, vol. 14(2), pp. 1262-1267, 1979.